Title

Numerical analysis of experimental studies of methane hydrate formation in a sandy porous medium

Authors

Yin, Zhenyuan
Moridis, George
Tan, Hoon Kiang
et al.

Publication Date

2018-06-01

DOI

10.1016/j.apenergy.2018.03.075

Peer reviewed

Numerical analysis of experimental studies of methane hydrate formation in a sandy porous medium

Author links open overlay panel ZhenyuanYin[ab] GeorgeMoridis[cda] Hoon KiangTan[b] PraveenLinga[a]
Show more

https://doi.org/10.1016/j.apenergy.2018.03.075 Get rights and content

Highlights

- MH formation via excess-water method was numerically analyzed using T+H v1.5.
- MH formation is determined as a kinetic reaction with dominant thermal processes controlling MH formation.
- Flow, thermal, and kinetic rate parameters are optimized using a history-matching technique.
- The spatial distributions of various phases at the end of the MH formation are strongly heterogeneous.

Abstract

We analyse numerically an earlier experimental study that involved the formation of methane hydrates by the excess water method in a small reactor filled with a sandy porous medium, and seek to address questions about the type of the hydration reaction and the phase heterogeneity in the resulting hydrate-bearing sand. Using a fine discretization describing the reactor assembly, the experimental process is faithfully replicated numerically. The multi-stage process of hydrate formation is subdivided in 7 steps. The experimental data from the continuously-monitored pressure and temperature during each step are used for comparison against the numerical predictions, the identification of the dominant processes and the determination of the associated parameters through a history-matching process that minimizes deviations between observations and simulation results. The results of this first-ever study on this subject demonstrate unequivocally that the hydration reaction is a kinetic (as opposed

to an equilibrium) process, and that the spatial distributions of the various phases (aqueous, gas and hydrate) at the end of the formation process are strongly heterogeneous. This has serious implications in simulation studies of hydrate dissociation that assume uniform initial phase saturation distributions. The history-matching process indicates that (a) the system behaviour is sensitive to some flow parameters (porosity and irreducible water saturation) only during the first water injection, (b) it is insensitive to the sand intrinsic permeability during all steps of the study, and (c) thermal processes dominate after the first water injection, yielding estimates of the thermal properties of the sand and of time-variable key parameters of the kinetic reaction.

Graphical abstract

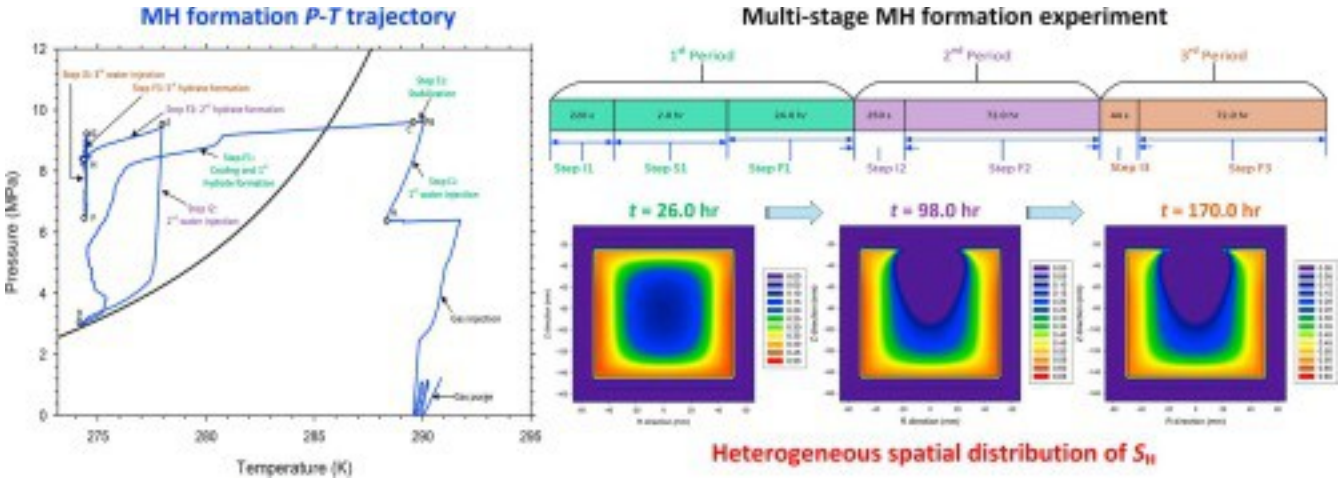

1. Download high-res image (238KB)
2. Download full-size image

- **Previous** article
- **Next** article

Keywords

Methane hydrate
Hydrate formation
Kinetic reaction
Porous medium
Numerical modelling
TOUGH+Hydrate v1.5
Heterogeneous

1. Introduction

1.1. Background

Gas hydrates are solid crystalline compounds that consist of water and gas molecules. The water molecules form cage-like crystal lattices (through hydrogen bonds), which encage guest gas molecules that are stabilised by the van der Waal's forces. The typical size of guest gas molecules that can fill the hydrate cages varies between 3.8 and 6.95 Å [1], [2]. Common gases in naturally occurring hydrates include hydrocarbon molecules (e.g. CH_4, C_2H_6, C_3H_8), as well as other gases, mainly H_2S, N_2 and CO_2, etc. Depending on the hydrate cavity number, structure and guest molecule size, there are three primary gas hydrate structures: namely, the cubic structure I (sI), the cubic structure II (sII) and the hexagonal structure H (sH) [3]. In general, gas hydrates are stable at suitably low temperatures *T* and high pressures *P*. They are non-flowing crystalline ice-like solids that can store effectively large amounts of gases. For example, 1 volume of methane hydrate (MH) can store 160–180 volumes of CH_4 gas under *STP*[4].

CH_4 is by far (in overwhelming abundance, actually) the most common hydrate-forming gas of naturally occurring hydrates. Pure CH_4 under suitable conditions forms sI type of hydrate as described by the following hydration reaction:

(1)CH4+NHH2O=CH4·NHH2O+QH

where N_H is the hydration number and typically varies between 5.75 and 6.2 for MH and Q_H is the associated enthalpy (measured to be 54.44 kJ/mol [5]) of the hydrate formation/dissociation reaction. The equilibrium pressure-temperature relationship of the $CH_4 + H_2O$ system is shown in the phase diagram of Fig. 1[6]. The four main dissociation methods are: (i) depressurization, in which the pressure (*P*) is lowered below the hydrate equilibrium pressure (P_{eq}) at the prevailing temperature (*T*), (ii) thermal stimulation, in which temperature (*T)* is raised above the hydrate equilibrium temperature (T_{eq}) at the prevailing *P*, (iii) the use of chemical inhibitors (salts or alcohols), which shifts the hydrate P_{eq}–T_{eq}equilibrium [2] and (iv) the use of CO_2 (and possibly other gases, such as N_2) to exchange CH_4 in hydrates [7]. It is also possible (and often advisable) to use combinations of the aforementioned production methods [8].

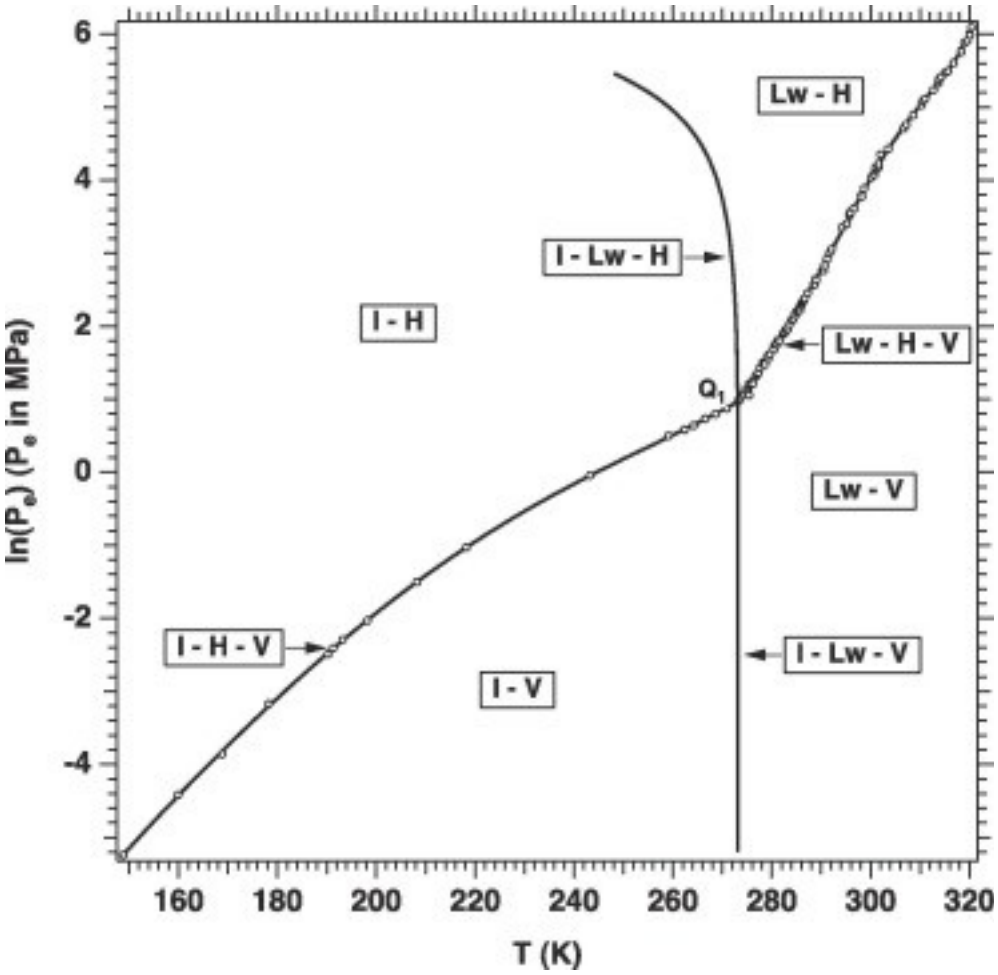

1. Download high-res image (152KB)
2. Download full-size image

Fig. 1. Pressure-temperature equilibrium relationship in the phase diagram of the $CH_4 + H_2O$+MH system in T+H showing all possible thermodynamic states [93].

1.2. Hydrates as an energy source

The preponderance of CH_4 in natural gas hydrates and the early realization [5] that these occur in vast amounts raised the issue of exploiting them as an energy source. Thus, there has been a considerable effort to estimate the amount of hydrocarbon gas hydrates resource on a global scale as the necessary first step in their exploitation. The estimates of the total amount of recoverable CH_4 from MH have varied tremendously over the years, ranging from 10^6 trillion cubic meter (TCM) [9] to 10^4 TCM [10], [11], [12], [13], [14], [15] to 10^3 TCM [16], [17]. These estimates are almost invariably the results of various models that are based on different evaluation criteria, and the uncertainty on the subject is substantial because the number of true physical surveys is very limited and insufficient to reach authoritative results. However, the

general consensus is that the worldwide quantify of hydrocarbon gas hydrates is vast and easily exceeds not only all the conventional natural gas reserves of 186.6 TCM [18], but also all hydrocarbon reserves. The amount is so large that even if a fraction of the total CH_4 trapped in hydrates is recoverable, it represents a very large resource that demands evaluation as a potential source of energy. This is further reinforced by the environmental desirability of CH_4because of its lower CO_2 release upon combustion, and by the growing global energy demands [8], [19]. Exploring MH reservoirs for energy recovery have attracted ever-increasing research and industry interests in several countries (e.g. USA, Canada, Japan, India, China, S. Korea, Singapore, etc.) [20]. Since the first report of hydrates contributing to gas production from the Messoyakha gas field in Russia [21], there have been several worldwide geological surveys and a limited number of field production tests. The main objectives of geological surveys are threefold: (a) to identify the locations of gas hydrate reservoirs and test the validity of geologic and geochemical models supporting the MH formation; (b) to estimate the volume of gas stored in the hydrate bearing sediments (HBS); and (c) to extract cores from HBS for testing and characterization of their properties. Major geological surveys over the last twenty years include the Ocean Drilling Program (ODP) Leg 204 [22] on the continental slop offshore Oregon (USA), the Integrated Ocean Drilling Program (IODP) Leg 311 on the northern Cascadia margin (USA) [23], ODP Leg 164 in Blake Ridge sediments (USA) [24], the Joint Industry Project (JIP) Leg I and II expeditions in the Gulf of Mexico (USA) [25], the Guangzhou Marine Geological Surveys (GMGS) in the north slope of the South China Sea (China) [26], the India National Gas Hydrate Program (NGHP) expeditions off the eastern cost of India (India) [27], the Ulleung Basin Gas Hydrate (UBGH) drilling expeditions in South Korea [28] and the drilling and coring programs planned by Ministry of Economy Trade and Industry (METI) in the Nankai Trough (Japan) [29]. A combined summary of the aforementioned geological surveys along with its findings is reported by Collett et al. [30].

These efforts have provided a wealth of information on the occurrence of MH in nature and resulted in several successful gas production field tests from permafrost-associated and marine hydrate deposits. These include: (a) the gas production tests at the Mallik site at the Mackenzie River Delta in Northwest Territories, Northern Canada in 2002 (involving thermal stimulation of a hydrate deposit) [31] and in 2007–2008 (involving depressurization-induced dissociation of a separate hydrate layer) [32]; (b) the Mount Elbert Well at the Alaska North Slope (USA) in 2007 (involving depressurization-induced dissociation) [33]; (c) the Ignik-Sikumi field trials at the Alaska North Slope (USA) in 2012, which involved both (i) a shorter-term CH_4 exchange with a CO_2/N_2mixture, as well

as (ii) a longer-term depressurization [34], and two recent depressurization-based production tests from offshore deposits: (d) the Nankai Trough test in 2013 (Japan) [35] and (e) the test in the Shenhu area of the South China Sea in 2017 (China) [36], [37]. These field tests have demonstrated the potential of gas production from hydrate reservoirs using conventional production technologies.

1.3. Laboratory studies on gas hydrates and knowledge gaps

Our fundamental understanding of the behaviour of naturally occurring HBS and the associated release and production of reservoir fluids has improved significantly as a result of the aforementioned surveys and field tests. However, significant knowledge gaps persist, and these cannot be easily addressed by field tests because of their limited number and very high cost, given the inhospitable locations of natural hydrate occurrences. To date there have been only 5 completed field production tests spanning across 15 years. Laboratory studies of retrieved HBS core samples from field studies have tried to address the issue. These studies have examined the HBS morphologies (e.g. pore-fill, lenses/veins, and nodules/chunks) [38], [39] and characterized their physical properties [40], [41], [42]. In addition, hydrate dissociation and gas production experiments and numerical analysis had been carried out using extracted hydrate cores from the NGHP-01 and the Mount Elbert sites [43]. A persistent problem is that these cores of naturally occurring HBS for laboratory studies have been very limited in number and are invariably disturbed.

Given the substantial challenges of extracting intact/undisturbed hydrate cores and by the general lack of prior knowledge on naturally occurring HBS, the associated knowledge gaps need to be addressed in laboratory studies involving synthetic gas hydrate. Such laboratory studies are necessary to characterize their thermophysical and geomechanical properties of hydrates and of HBS (e.g., density, hydration number, thermal conductivity, specific heat, heat of formation and dissociation, stress, strain, Poisson's ratio, Young's moduli and stiffness, etc.) [44], [45], to analyse their dissociation process and the associated production of gas and water under controlled conditions (a difficult proposition in field studies) [46], [47]. In addition, a few kinetic models are proposed with a number of numerical studies carried out to simulate the methane hydrate formation and dissociation kinetic behaviour [48], [49], [50], [51]. A comprehensive review of these gas hydrate formation [52], [53] and dissociation kinetic models together with reservoir simulators [54] were reviewed in our earlier papers.

Obviously, the first step in such laboratory studies is the formation of representative hydrates in porous media. Several techniques have been devised to synthesize HBS in

reactors during the past two decades. The four main hydrate-forming methods in the open literature are: (a) ice-to-hydrate method [55], [56], [57], [58]; (b) the excess-gas method [59], [60], [61]; (c) the excess-water method [62], [63], [64], [65]; and (d) the dissolved-gas method [66], [67], [68]. A schematic of the four formation processes in relation to the $CH_4 + H_2O$ phase diagram is shown in Fig. 2.

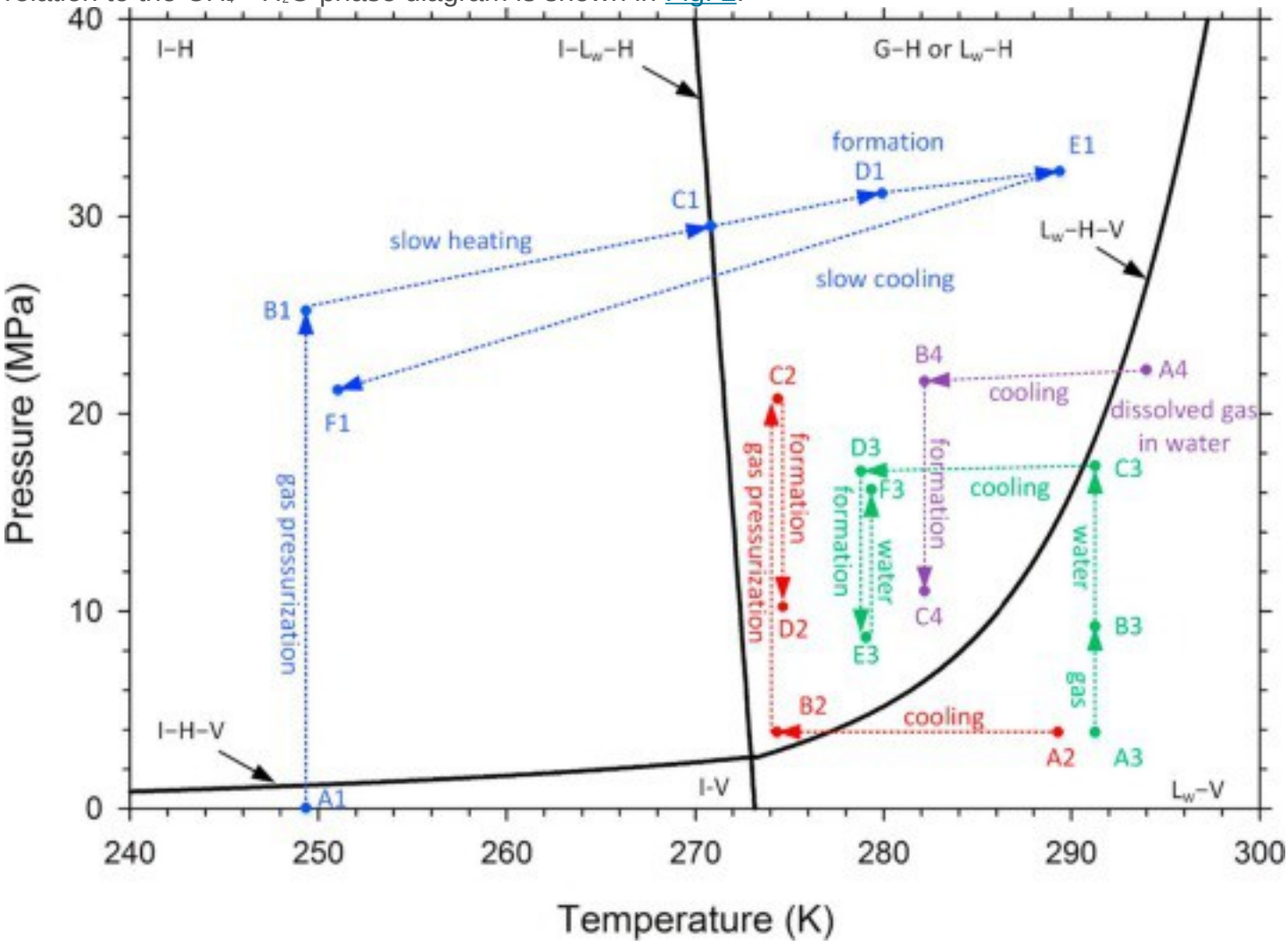

1. Download high-res image (144KB)
2. Download full-size image

Fig. 2. Schematic *P-T* trajectory during MH formation by various methods in relation to the $CH_4 + H_2O$+MH phase curve: (i) A1-F1 (in blue) refers to ice-to-hydrate method [57]; (ii) A2-D2 (in red) refers to excess-gas method [59]; (iii) A3-F3 (in green) refers to excess water method [62]; (iv) A4-C4 (in purple) refers to dissolved gas method [67]. (For interpretation of the references to colour in this figure legend, the reader is referred to the web version of this article.)

The ice-to-hydrate formation method was proposed by Stern et al. [55], [56], [57], [58] and has not been used in HBS laboratory studies because it involves mechanical mixing of ice with sand, i.e., there is no hydrate formation in situ within the matrix of a porous medium. The excess-gas method that was first proposed by Handa and Stupin [59] is the most commonly used experimental method to form gas hydrates in laboratories and there are indications that it leads to cementing of sandy sediments [69]. Linga et al. [61]investigated the behaviour of CH_4-hydrate formation created by this method in sandy media. Other studies involving hydrate formation by the same method investigates several aspects of the process, e.g., the effect of porous media type and grain size [70], [71], aqueous phase saturation (S_A) [72], salt concentration [73], and reactor configuration [74], [75]. Only one of these excess-gas studies [61] mentions heterogeneity in the spatial distribution of the hydrate saturation (S_H) formed in the porous media, and this is done only in qualitative terms. Quantitative analyses of $S_H$heterogeneity are discussed only in the studies of Kneafsey et al. [43], [76] because these had the benefit of high-definition X-ray Computed Tomography (CT) scanning in addition to other standard laboratory equipment. The dissolved-gas method was used for the study of formation behaviour of MH by Spangenberg and Waite [67], [77] with a pore-filling type of hydrate reported. The spatial distribution of S_H during CH_4-hydrate formation by this method in a large reservoir simulator (LARS) was discussed by Mike et al. [68], [78] using Electrical Resistivity Tomography (ERT) technique, and showed high S_H accumulations in the boundary regions exposed to active cooling.

In this study, we focus on the numerical analysis of the excess-water technique used in the underlying laboratory experiments [63]. This technique was first proposed by Priest et al. [62] and is claimed to result in a pore-filling type of more homogeneously-distributed (than in other methods) hydrates, but has not been widely used. Later, Falser et al. [65] used this method to produce artificial HBS samples for the numerical simulation of dissociation experiments, but they used the average value of $S_H = 40\%$ without considering spatial heterogeneity. The experimental study of Kneafey et al. [79] used X-ray CT scanning to show that heterogeneities in the S_H of hydrates formed in porous media depended on the location of the trapped gas. In recent studies, Yang et al. [80], [81], [82] used the Magnetic Resonance Imaging (MRI) technique to compare the water saturation (S_A) distributions of HBS formed by both the excess-gas and the excess-water methods, and revealed consistently heterogeneous S_A (and, by inference, heterogeneous S_H) distributions.

A common conclusion from the limited number of studies of CH_4-hydrate formation in reactors is that the spatial distribution of $S_H$tends to be heterogeneous. This is a consistent observation confirmed by all visualization/quantification techniques used in the studies, i.e., X-ray CT-scanning [76], [83], [84], ERT [68], [78] and MRI [71], [80], [85], [86]. However, during most hydrate property characterization tests, dissociation experiments and numerical modelling studies, one assumption commonly made is that the initial S_H spatial distribution is homogeneous in the reactor or testing vessel [47], [87], [88], [89], [90].

The aforementioned evidence from visualization experiments raises serious concerns about the validity of this assumption, which can lead to erroneous interpretation of the experimental data. Actually, this was an important conclusion of our previous numerical study [91] on the same set of experiments analysed here (involving thermally-induced MH dissociation), and is a major impetus for the current study. The other conclusion from that study [91] was that there were significant indications that the hydrate formation and dissociation reactions in a 1.0L reactor could not be adequately described by the assumption of an equilibrium formation/dissociation reaction, and that the possibility of kinetic reactions needs to be considered and the associated parameters be evaluated. The current study intends to address these issues, covering the entire spectrum from the multi-stage hydrate formation (covered in this paper) to the dissociation of the hydrate sample (to be discussed in a subsequent paper). To our knowledge, this is the first simulation study that analyses laboratory experiments involving artificial HBS and covers concurrently the issues and effects of phase heterogeneity and equilibrium vs. kinetic behaviour.

1.4. Objectives and the role of numerical simulation

The overall objective of this paper (the first in a series of two papers) is to duplicate numerically and analyse an earlier laboratory experiment [63] involving hydrate formation by the excess-water technique. The specific objectives of the study are directly associated with the conclusions and suggestions for further study stated in the paper of Yin et al. [91] and involve the use of the experimental data in [63] as the basis for

(1)

The numerical investigation of whether the reactions of the several stages of hydrate formation in that experiment can be described by an equilibrium or a kinetic model.

(2)
The determination of the relative importance and of the values of various parameters (thermal, flow, kinetic if the hydrate formation is shown to be governed by a kinetic reaction, etc.) by using an optimization (history-matching) process [92] that minimizes the deviations between the laboratory measurements and numerical predictions.

(3)
The development of estimates of the heterogeneous spatial distribution of the various phases (hydrate, aqueous and gas) at the end of the hydrate formation process, to be used as an input in the analysis of the dissociation experiment that is covered in the next paper of this series. In the absence of the highly-specialized CT-scanning equipment that can describe accurately and conclusively the spatial distributions of these phases (and the almost inevitable heterogeneities), numerical simulation constrained by additional laboratory data (e.g., the evolution of P and T at appropriate locations within a reactor) has the potential to be a powerful alternative, or even substitute. This study aims to evaluate this proposition.

2. The underlying laboratory studies

In this section, we present a summary of the laboratory studies that provided the data for our numerical analysis. The interested reader is directed to the study of Chong et al. [63] for a detailed description of the experimental study.

2.1. Experimental apparatus and materials

Fig. 3 shows a schematic of the cross section view of the hydrate reactor, the dimensions of which are described in Table 1 with a picture of the hydrate reactor shown in Fig. S1 in supporting information. It consists of a 1.0 L fixed bed reactor blanketed by a cooling jacket that circulates a heat exchange fluid through a 15.0 L circulating bath that can provide a constant temperature in the range between 243.2 K and 443.2 K. The maximum design pressure of the reactor is 10.0 MPa. A stainless-steel nozzle at the top centre of the reactor is used for water injection during hydrate formation and fluids production during hydrate dissociation experiments. Two sets of Rosemount SMART pressure transmitters (Model 3051S) are installed for pressure P measurement at the inlet and outlet of the reactor. The temperatures (T_a and T_b) at the reactor locations shown in Fig. 3 are measured by two sets of six-point thermocouples (with an accuracy of 0.1 K). During the experiment, P and T data were

recorded continuously using a data acquisition system. Fig. S2 in supporting information presents a detailed schematic of the entire set of the experimental apparatus.

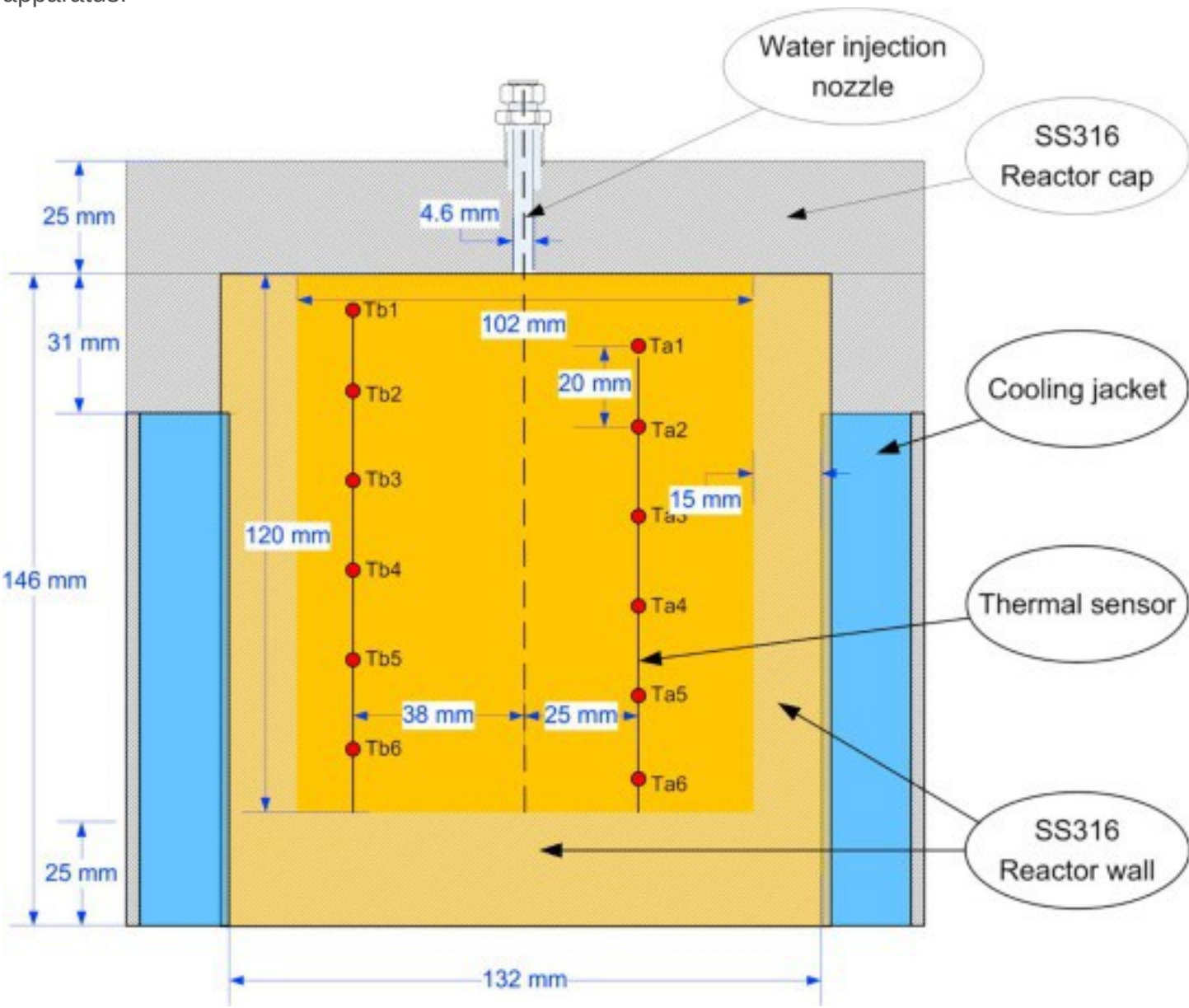

1. Download high-res image (257KB)
2. Download full-size image

Fig. 3. Cross section view of the reactor for methane hydrate formation in sandy sediment experiments with simulation domain (shaded in orange). (For interpretation of the references to colour in this figure legend, the reader is referred to the web version of this article.)

Table 1. Geometry of the reactor used in the methane hydrate formation experiment.

Parameter	Value
Internal height of reactor	120.0 mm
Internal diameter of reactor	102.0 mm
Internal volume of reactor	0.98 L
External height of reactor	170.0 mm
External diameter of reactor	132.0 mm
Thickness of reactor wall	15.0 mm
Thickness of reactor top and bottom	25.0 mm
External diameter of pressure outlet	9.52 mm
Internal diameter of pressure outlet	4.60 mm
Material of reactor	SS316

The laboratory study used methane gas with a purity of 99.9% and de-ionized water. The porous medium was a uniform fine silica sand with a quartz content of over 99.0%, a 97% mean particle diameter between 150 μm and 300 μm and a grain density of 2.65 g/cm^3. The absolute permeability of the unconsolidated packed sediment was 3.83 Darcy, as measured from a mercury porosimetry test. A differential scanning calorimetry test determined that the specific heat of the dry sand was 1400 J/kg/K. The heat exchange fluid was a mixture of water and glycol.

2.2. Sample preparation and hydrate formation

The entire hydrate formation process lasts for around 170.0 h. To form hydrate, the hydrate reactor was first filled with 1480.5 g of sand which, after compaction, resulted in a porosity $\phi = 0.44$. The reactor was then sealed and slowly purged three times with CH_4gas in order to remove the residual air. The reactor was subsequently pressurized with CH_4 gas and was allowed to stabilize for around three hours to a final $P = 6.35$ MPa and $T = 288.2$ K. These were the initial P and T conditions for the ensuing hydrate formation process, which proceeded in three periods that involved a total of 7 consecutive steps. These were the following:

1st Period, Injection Step 1 (Step I1): De-ionized water was injected into the reactor at a flow rate of 50 mL/min for 220 s, corresponding to a total volume of 183.3 mL water.

1st Period, Stabilization Step 1 (Step S1): This step lasted 2.0 h, during which time the injected water and gas in the reactor were re-distributed and reached a steady state.

1st Period, Hydrate Formation 1 (Step F1): This step lasted 24.0 h and involved 2 intervals. In the first shorter interval (lasted 0.66 h), the temperature of the circulating refrigerating fluid was reduced to a final level, $T = 274.0$ K that was sufficiently low to

create hydrate-formation conditions. This *T* was maintained constant during the second longer interval (23.34 h). Given the rate of heat transfer between the cooling fluid and the interior of the reactor, it was expected that most of the CH_4-hydrate formation occurred during the 2nd interval (an issue to be investigated numerically).

2nd Period, Injection Step 2 (Step I2): During this step, 208.3 mL of water were injected for 250 s, i.e., at a constant flow rate of 50 mL/min.

2nd Period, Hydrate Formation 2 (Step F2): This step lasted 72.0 h. During the entire 2nd period (Steps I2 and F2), the temperature of the heat-exchange fluid was maintained constant at the level attained in Step F1.

3rd Period, Injection Step 3 (Step I3): During this step, water was injected at a flow rate of 30 mL/min for 44 s, for a total of 22.0 mL of injected water.

3rd Period, Hydrate Formation 3 (Step F3): This step also lasted 72.0 h. As in Period 2, the temperature of the heat-exchange fluid was maintained constant at the level attained in Step F1. The hydrate formation was deemed complete at the end of Step F3, whereby the pressure drop per hour was negligible (0.0036 MPa/hr) and consistent over a longer period of time (40.0 h).

A schematic timeline of the aforementioned periods and steps is presented in Fig. 4. Fig. 5a shows the *P-T* conditions at the beginning and end of the various steps on the $CH_4 + H_2O$ phase diagram, as well as the associated trajectory of the changes obtained with a *P/T* acquisition frequency of 20 s. Table 2 lists the *P*and *T* conditions at the beginning and end of each period and step, and Table 3 summarizes the flow rates, duration, and cumulative volumes of water injection during steps I1, I2 and I3. Fig. 5b presents the evolution of the measured temperature of the heat-exchange fluid in the first interval of Step F1, and serves as the time-dependent boundary condition in the ensuing simulations. Note that the *T* of the heat-exchange fluid remains constant for the remainder of the experiments, i.e., in the 2nd interval of Step F1, and during Steps I2, F2, I3 and F3.

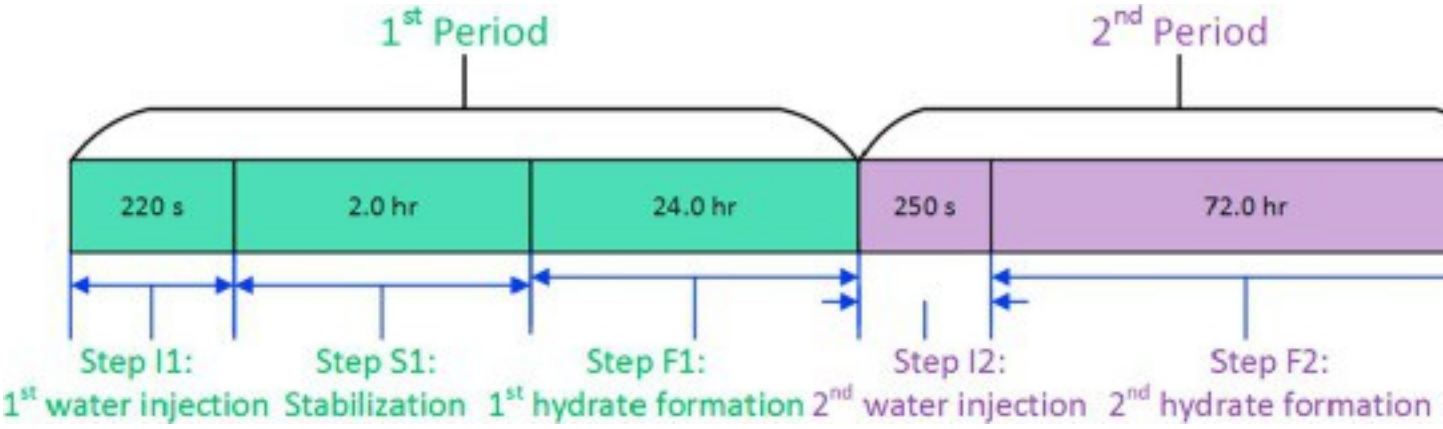

1. Download high-res image (99KB)
2. Download full-size image

Fig. 4. Timeline of MH formation periods and individual steps (not to scale).

(a)

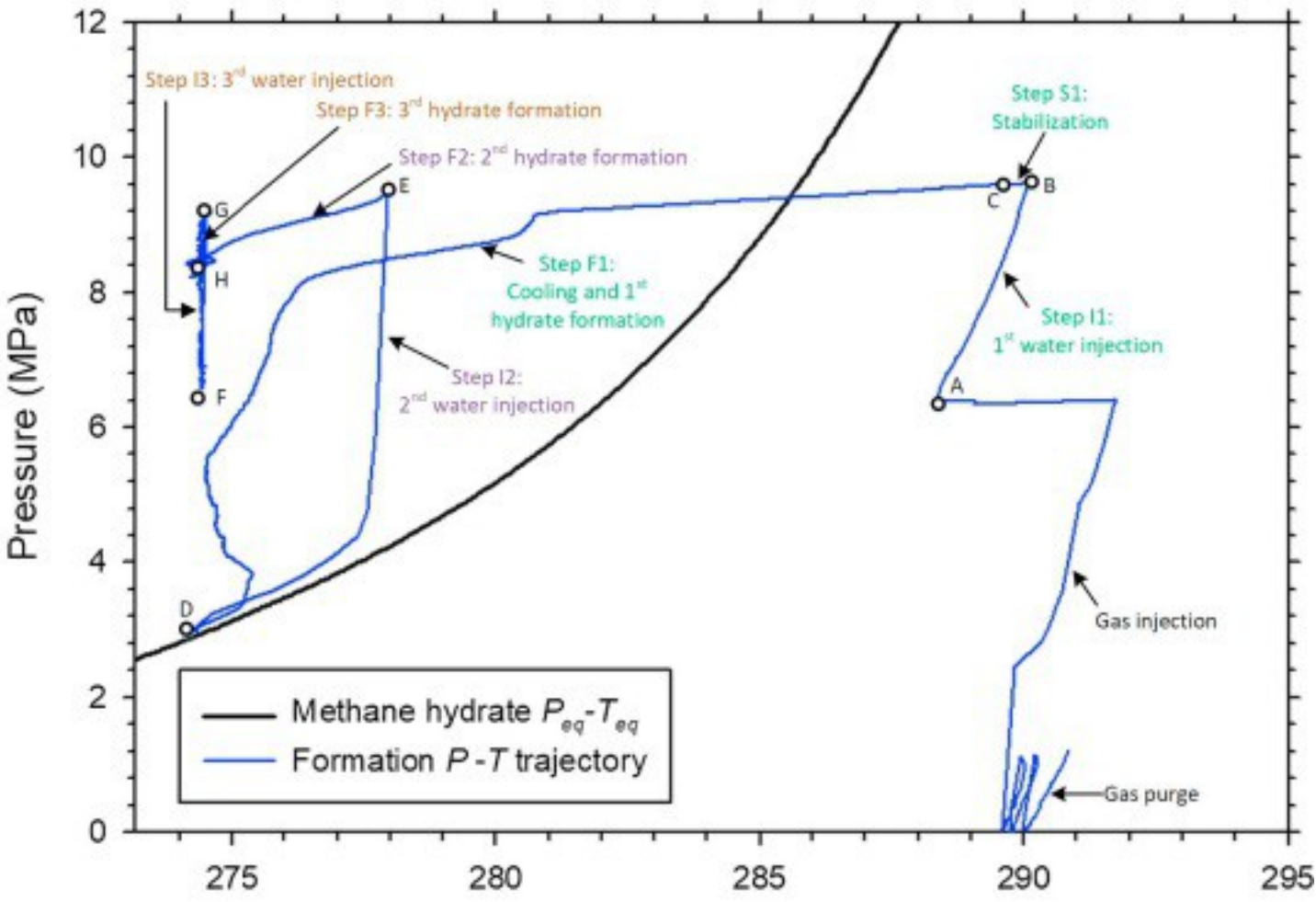
Step I3: 3rd water injection
Step F3: 3rd hydrate formation
Step F2: 2nd hydrate formation
Step S1: Stabilization
Step F1: Cooling and 1st hydrate formation
Step I1: 1st water injection
Step I2: 2nd water injection
Gas injection
Gas purge
A
B
C
D
E
F
G
H
Methane hydrate P_{eq}-T_{eq}
Formation P-T trajectory
Pressure (MPa)
0
2
4
6
8
10
12
275
280
285
290
295

(b)

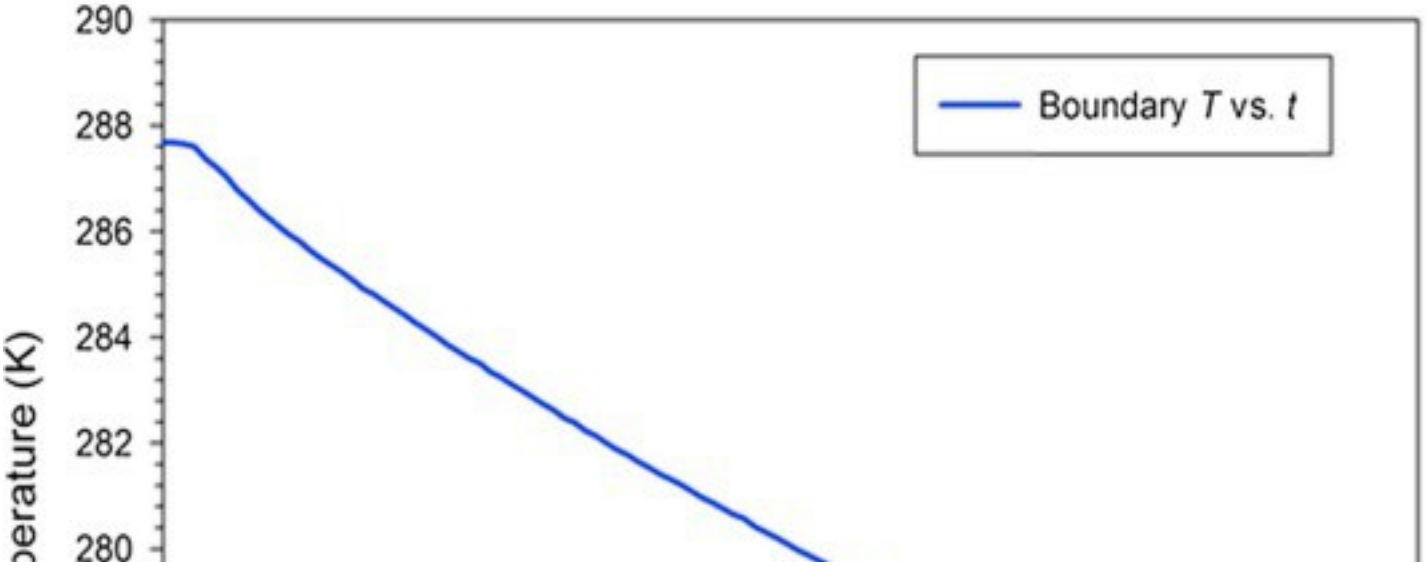
Boundary T vs. t
280
282
284
286
288
290

1. Download high-res image (230KB)
2. Download full-size image

Fig. 5. (a) *P*-*T* trajectory during MH formation experiment analysed in this study. (b) Boundary (circulating heat-exchange fluid) temperature evolution against time in Step F1. *T* remains constant at its final level for $t > 0.66$ h.

Table 2. *P* and *T* conditions at the beginning and end of each period and step.

Period	Step	Initial *P*(MPa)	Final *P*(MPa)	Initial bath *T*(K)	Final bath *T*(K)
1st Period	I1	6.3	9.6	288.2	288.2
	S1	9.6	9.5	288.2	288.2
	F1	9.5	3.2	288.2	274.5
2nd Period	I2	3.2	9.5	274.5	274.5
	F2	9.5	6.5	274.5	274.5
3rd Period	I3	6.5	9.5	274.5	274.5
	F3	9.5	8.7	274.5	274.5

Table 3. The properties of water injected into the hydrate reactor during formation.

No. of H_2O Injection	Conditions			
	Temperature (K)	Rate (ml/min)	Duration (s)	Volume (ml)
Step I1	296.2	50	220	183.33
Step I2	296.2	50	250	208.33
Step I3	296.2	30	44	22.00

3. The numerical model and the simulation approach

3.1. The T+H numerical model

The simulations in this study were conducted using the T+H code [6], [93], a numerical simulator developed at the Lawrence Berkeley National Laboratory (LBNL) to model the non-isothermal CH_4release, phase behaviour and flow under conditions typical of CH_4-hydrate deposits (i.e., in the permafrost and in deep ocean sediments, as well in any laboratory experimental set-up) by solving the coupled equations of fluids and heat balance associated with such systems. The simulator can model all the known processes involved in the system response of CH_4-hydrates in complex geologic media, including the flow of fluids and heat, the thermophysical properties of reservoir fluids, the thermodynamic changes and phase behaviour, and the non-isothermal chemical reaction of CH_4-hydrate formation and/or dissociation, which can be described by either an equilibrium or a kinetic model. T+H is a fully implicit compositional simulator, and its

formulation accounts for heat and the various mass components that are partitioned among four possible phases: gas, aqueous liquid, ice, and hydrate. The T+H code can describe all the 15 possible thermodynamic states (phase combinations) of the $CH_4 + H_2O$ system (see Fig. 1) and any combination of the three main hydrate dissociation methods: depressurization, thermal stimulation and the effect of inhibitors. It can handle the phase changes, state transitions, strong nonlinearities and steep solution surfaces that are typical of hydrate formation and dissociation problems. A detailed description of the code, its underlying physics and capabilities, of the numerical techniques and of the various options it provides can be found in the User's manual report written by Moridis [6].

When hydrate formation/dissociation is treated as a kinetic reaction, the maximum number of mass components is 4, i.e., H_2O, CH_4, CH_4-hydrate and an optional water-soluble inhibitor such as a salt or an alcohol. For an equilibrium reaction, the CH_4-hydrate is not considered a separate chemical compound (component) but only a state of the H_2O–CH_4 system and, consequently, the maximum number of mass components is 3: H_2O, CH_4, and an optional water-soluble inhibitor. As is obvious, the kinetic model is computationally more demanding as it involves consideration of an additional mass balance equation per element of the discretized domain.

Earlier work [94] indicated that the treatment of hydrate formation and dissociation as an equilibrium reaction is appropriate in long-term processes (such as gas production from hydrate deposits over long periods), whereas a kinetic consideration is better suited to short-term processes (not exceeding a few days) and mild formation-inducing driving forces. As indicated earlier, in our work here we investigate whether the reactions in the underlying laboratory study were kinetically retarded or simpler equilibrium processes.

3.2. Simulation domain and discretization

We used the MeshMaker v1.5 application [95] to construct the grid of the 2D axi-symmetric cylindrical simulation domain (shown in Fig. 6) that accurately described the geometry of the hydrate reactor. For maximum accuracy, and from the experience gleaned from previous simulation studies [96], [97], [98], [99], [100], [101], [102], [103], we used a very fine spatial discretization. The internal radius of the reactor ($r = 51.0$ mm) is discretized into 26 (mostly uniformly-sized) subdivisions ($1 \times \Delta r = 1.0$ mm and $25 \times \Delta r = 2.0$ mm), and the reactor wall thickness ($d_{wall} = 15.0$ mm) is discretized into 5 additional uniform subdivisions ($5 \times \Delta r = 3.0$ mm). One additional outermost subdivision ($\Delta r = 0.1$ mm) is added to describe the both the time-dependent heat-exchange boundary, as well as the no-flow boundaries of the insulated reactor walls (see Fig. 3).

The internal height of the reactor ($d = 120.0$ mm) is discretized into 48 uniformly-sized subdivisions in z ($48 \times \Delta z = 2.5$ mm). In addition, the thickness of the top and bottom boundaries of the reactor ($d_{top} = d_{bot} = 25.0$ mm) is each discretized into 5 uniform subdivisions ($5 \times \Delta z = 5.0$ mm). In total, the cylindrical simulation domain was discretized into $32 \times 58 = 1856$ elements (gridblocks) in (r, z). The fine discretization is important in the effort for accurate predictions in the small reactor of the Chong et al. [51] system as it necessary to capture the steep fronts expected near the injection nozzle and the boundary walls of the reactor. Assuming no inhibitors (such as salt) in the system, the domain discretization results in 5568 and 7424 simultaneous equations for an equilibrium and a kinetic hydration reaction, respectively.

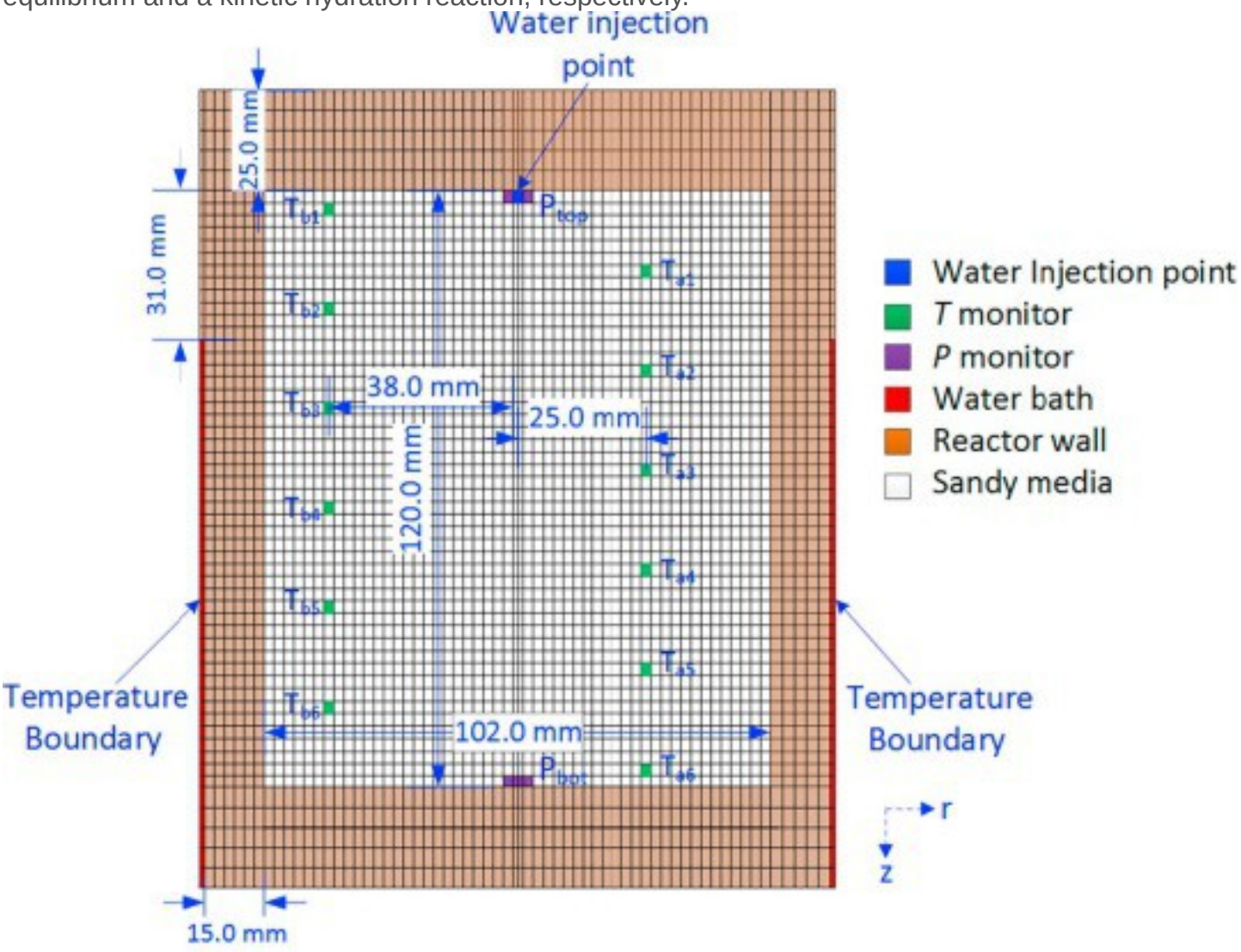

1. Download high-res image (293KB)
2. Download full-size image

Fig. 6. Simulation domain with mesh details used in the numerical simulation.

3.3. System thermophysical properties, initial and boundary conditions

Table 4 summaries the key thermophysical properties of the quartz sand used in the experiment, of the metal parts of the reactor, and the parameters for the constitutive models involved in the simulator. Note that some of the listed properties of the sandy porous medium originated from direct measurements from laboratory tests and are not parameters to be identified by a history-matching technique, thus reducing the uncertainties in the numerical estimates. The composite thermal conductivity model follows the model in Moridis [93]. In the absence of direct measurements, the parameter values of Table 4 that were used in the relative permeability [104] and the capillary pressure models [105], [106] were obtained in studies of sandy materials that are appropriate analogues of the medium in the Chong et al. [63] studies and are shown in Figs. S3 and S4, respectively in the supporting information. The kinetic equation of hydrate formation follows the Kim-Bishnoi model [50]. It is noted that Kim-Bishnoi model was proposed originally to model hydrate dissociation kinetics in porous media. However, a number of numerical studies were carried out in the past to investigate the methane hydrate formation and dissociation behaviour in sandy medium employing the Kim-Bishnoi model with driving force defined as the fugacity difference between gas phase and hydrate equilibrium [49], [107]. Table 5 summarizes these kinetic rate model and the associated kinetic rate parameters employed in the numerical studies along with major assumptions and improvements. The associated kinetic parameters used in our study in Table 4 originate from previous simulation studies [94], [108], [109], and are used only as initial estimates that are adjusted through a history-matching process minimizing deviations between the experimental data and the numerical estimates of this study.

Table 4. Thermophysical properties of materials and parameters of constitutive models.

Parameter	Value
Gas composition	100% CH_4
Intrinsic permeability ($k_r = k_z$)	3.83 Darcy
Intrinsic porosity (ϕ)	0.44
Density of quartz sand (ρ_s)	2650 kg/m^3
Thermal conductivity of sand under dry condition ($k_{\theta d}$)	0.30 W/m/K
Thermal conductivity of sand under fully saturated condition ($k_{\theta w}$)	1.65 W/m/K
Specific heat of quartz sand (C_R)	1400 J/kg/ K
Thermal conductivity of SS316 ($k_{\theta s}$)	16.0 W/m/K

Parameter	Value
Specific heat of SS316 (C_s)	500 J/kg/ K
Composite thermal conductivity model (k_θ) [93]	kθ=kθd+SA1/2+SH1/2(kθw-kθd)
Relative permeability model (OPM model) [104]	krA=SA-SirA1-SirAnA
	krG=SG-SirG1-SirGnG
n_A	3.0
n_G	3.0
S_{irA}	0.20
S_{irG}	0.01
Capillary pressure model (OPM model) [105]	Pcap=-P0[(S∗)-1/λ-1]1-λ
	S∗=SA-SirASmxA-SirA
S_{irA}	0.115
λ	0.60
P_0 (Pa)	2×10^3
S_{mxA}	1.00
Hydrate dissociation kinetic rate [50]	nH=FAK0Aexp(-ΔERT)(feq-fg)
Hydration reaction constant (K_0)	3.6×10^4 mol/m² Pa s
Reaction surface area (A)	Computed internally (see Moridis [6])
Surface area adjustment factor (F_A)	1.0
Activation energy (ΔE)	81.0 kJ/mol

Table 5. Summary of methane hydrate formation kinetic models employed in numerical studies.

Study	Hydrate formation kinetic model and kinetic rate parameters	Hydrate particle surface area in sandy medium (A_s) (m²/m³)	Key Assumptions
Sun and Mohanty [49]	nH=K0Asexp(-ΔERT)(feq-fg) ΔE = 81.08 kJ/mol $K_0 = 5.9 \times 10^{-11}$mol/m²·Pa·s (MH formation) $K_0 = 3.6 \times 10^4$mol/m²·Pa·s (MH dissociation)	AS=ΓApAp=ϕe3/2(2k)1/2,ϕe=(SA+SG)ϕΓ=SGSASH2/3	Following the approach of Yousif [48]with a modification on pore surface area
Moridis et al. [93]	nH=K0Asexp(-ΔERT)(feq-fg) ΔE = 89.7 kJ/mol $K_0 = 1.78 \times 10^6$mol/m²·Pa·s	AS=0.879FA1-ϕrpSH2/3rp=45k(1-ϕ)2ϕ31/2	Spherical hydrate particle in the voids of sandy porous medium

Study	Hydrate formation kinetic model and kinetic rate parameters	Hydrate particle surface area in sandy medium (A_s) (m^2/m^3)	Key Assumptions
Li et al. [107]	nH=K0Asexp(-ΔERT) (feq-fg) ΔE = 80.90 kJ/mol K_0 = 65.0 mol/m²·Pa·s	AS=0.8791-ϕrpSG2/3SAβ(1-SH)β $r_p = 3.75 \times 10^{-4}$ m	Following the approach of Moridis [93]with gas phase in pore voids contributing to hydrate formation
This work	nH=K0Asexp(-ΔERT) (feq-fg) ΔE = 81.00 kJ/mol $K_0 = 3.6 \times 10^4$mol/m²·Pa·s [110]	AS=0.879FA(t)1-ϕrpSH2/3rp=45k(1-ϕ)2ϕ31/2	Following the approach of Moridis [93]with $F_A$optimized as a function of time based on a history matching technique [92]

The initial and boundary conditions for all steps are as described in Section 2.2, in Fig. 5a and b, and in Table 2, Table 3. Obviously, the initial conditions at the beginning of every step in the three periods of the experiments and of the corresponding simulations are the conditions at the end of the previous one.

3.4. The simulation approach and output of simulation results

The modelling process duplicated numerically all the 7 steps in the three periods described in Section 2.2, and was designed to address the objectives discussed in Section 1.4. We initially attempted to determine whether the hydrate formation was an equilibrium process or kinetically retarded. The criterion for this determination was the degree of fit between the laboratory measurements and the numerical estimates of the evolution of pressure P and temperature T over time. Of the two, P was deemed more important because it was the parameter most responsive to hydrate formation (the T-response was expected to be slower for reasons described later). An equilibrium process represents the fastest possible reaction of hydrate formation: experimental measurements indicating a slower reaction despite thermal properties in an equilibrium model that are below the lower limits of values reported in the literature (selected to delay the reaction predictions) are a strong indication of a kinetic process.
We then attempted to determine the values of the critically important parameters affecting the formation of the CH_4-hydrates in the reactor. After several scoping calculations, we focused the parameter identification effort on the following variables: ϕ, S_{irA}, C_R, $k_{\theta w}$, F_A and N_H. These were treated as perturbation parameters that

were determined through the history matching process of Thomas et al. [92] that minimized the differences between observations and numerical predictions. The measurements used as the “ground truth” in the history-matching process include the evolution of T (T_a, T_b) and P (P_{top} and P_{bot}) at the locations identified in Fig. 6. The optimized parameter values were used for the estimation of the spatial distributions of the phase saturations. In the absence of direct visualization and quantification capabilities of the phase saturations (which can only be afforded by the use of specialized phase visualization equipment), these heterogeneous estimates offer the one of the limited possibilities to account for heterogeneity in the analysis of the hydrate dissociation in hydrate experiments.

Note that not all parameters were varied or estimated simultaneously in every step of the simulation for history matching: depending on the physical process of a particular step, some were fixed at values obtained from a previous step. An additional issue is that the surface area adjustment factor F_A is in essence an adjustment to the combined product of the kinetic reaction constant K_0 of the hydrate reaction and of the area of the reaction surface (Aestimated internally by the T+H model as a function of the S_H and the medium porosity, see Moridis [93]); the value of K_0 was kept constant at the level specified by Clark and Bishnoi [110]. $F_A$quantifies the area over which the hydrate reaction occurs, and its value can change during hydration as S_H, ϕ and the reaction surface (determined by non-zero fugacity differences in Eq. (2)) change.

(2)nH=FAK0Aexp-ΔERT(feq-fg)

The history-matching process in Step I1 of the study (see Section 4.1) allowed estimation of the values of ϕ and S_{irA} of the sand, parameters that were determined to control the system behaviour during the first water injection. Although ϕ and k had been experimentally determined, history-matching suggested (a) a need for adjustment only for ϕ during Step I1, and indicated that the system behaviour was practically insensitive to (b) the intrinsic permeability k during all steps of the study and (c) the wettability properties of the sand (relative permeability and capillary pressure) in all steps from S1 to F3 of the experiment, during which thermal processes dominated the system behaviour and their values were estimated. Thus, the measured k was used unaltered in the simulations and the history matching process did not consider any hydraulic properties after the determination of ϕ and S_{irA} in Step I1, focusing instead on the thermal properties. The limited dependence on the flow properties was expected because of the small reactor volume and the high intrinsic permeability k of the sand that limited any significant wettability effects and any associated flow retardation.

4. Simulation results and discussions

4.1. Step I1: 1st water injection

During this 220-s step, water at a temperature of $T = 296.2$ K was injected at a flow rate of 50 mL/min and P continuously increased from 6.35 MPa to 9.60 MPa because of the addition of the practically incompressible water to the reactor. We observe an excellent agreement of the evolution of the experimentally-obtained pressure (Fig. 7a) and temperature (Fig. 7b) over time during Step I1 with the numerical simulation estimates using optimized parameters ($\phi = 0.448$ and $S_{irA} = 0.12$).

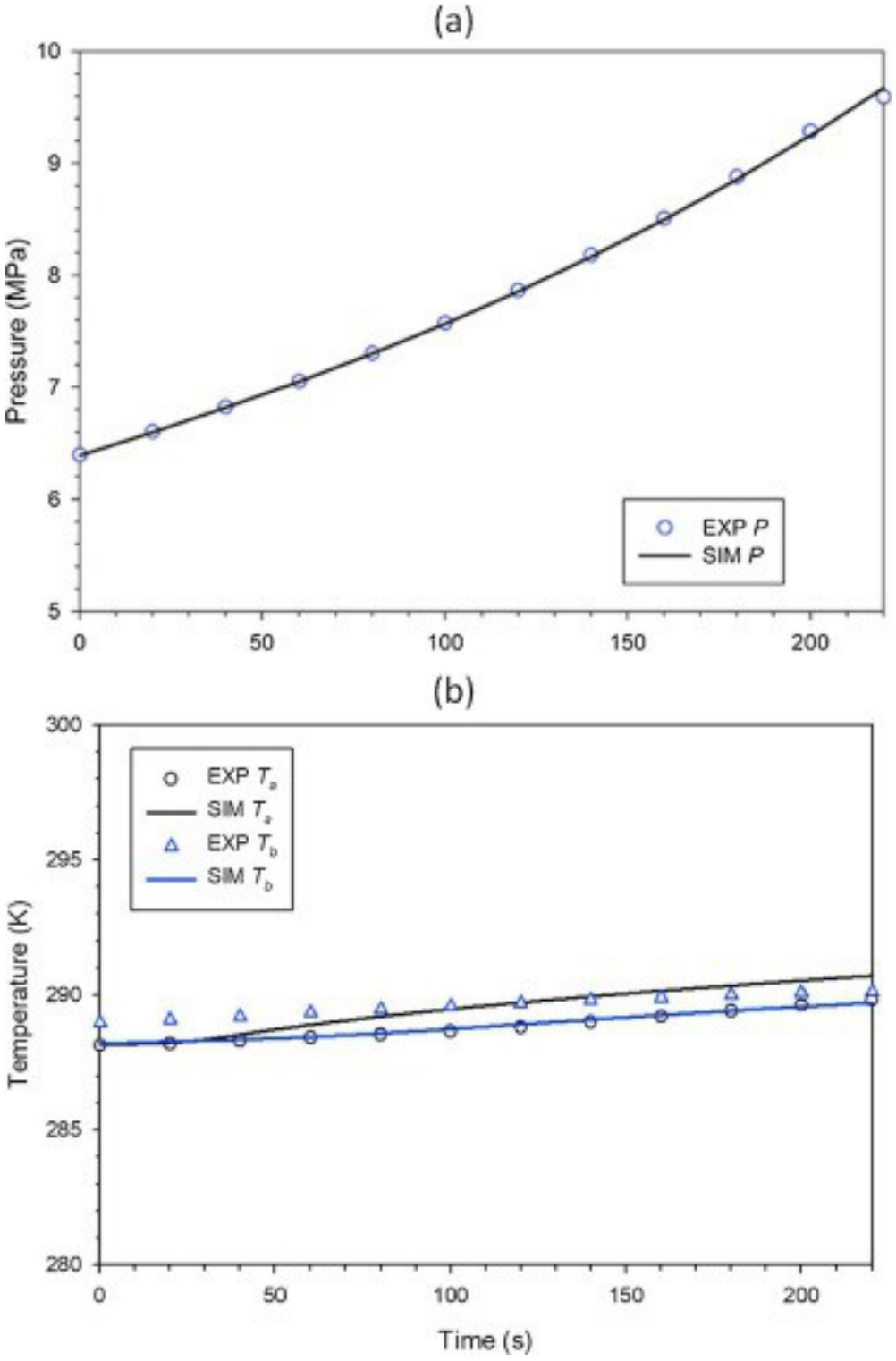

1. Download high-res image (97KB)
2. Download full-size image

Fig. 7. (a) Evolution of *P* over time during Step I1. (b) Evolution of *T* over time during Step I1.

Fig. 8 shows the spatial distributions of P, T, S_A and S_G at the end of Step I1. As expected, the distributions are symmetric about the z-axis at $r = 0$. The pressure $P = 9.6$ MPa is practically uniform in the reactor because of the high permeability of the porous medium and the small size of the reactor. This is not the case in the spatial distribution of T, which is higher near the injection nozzle (where the water warmer than the initial reactor temperature is injected), and gradually decreases both radially and vertically away from it. The S_A spatial distribution, and its complementary S_G distribution, (a) show accumulation of water in the upper part of the reactor because at the end of Step I1 there is insufficient time for drainage and S_A homogenization and (b) the S_A values are the highest in the vicinity of the injection nozzle and decline with an increasing distance from it. Note that, despite the higher T of the injected water, the S_A and T distributions do not coincide because of heat exchange between the advancing H_2O front and the cooler porous medium.

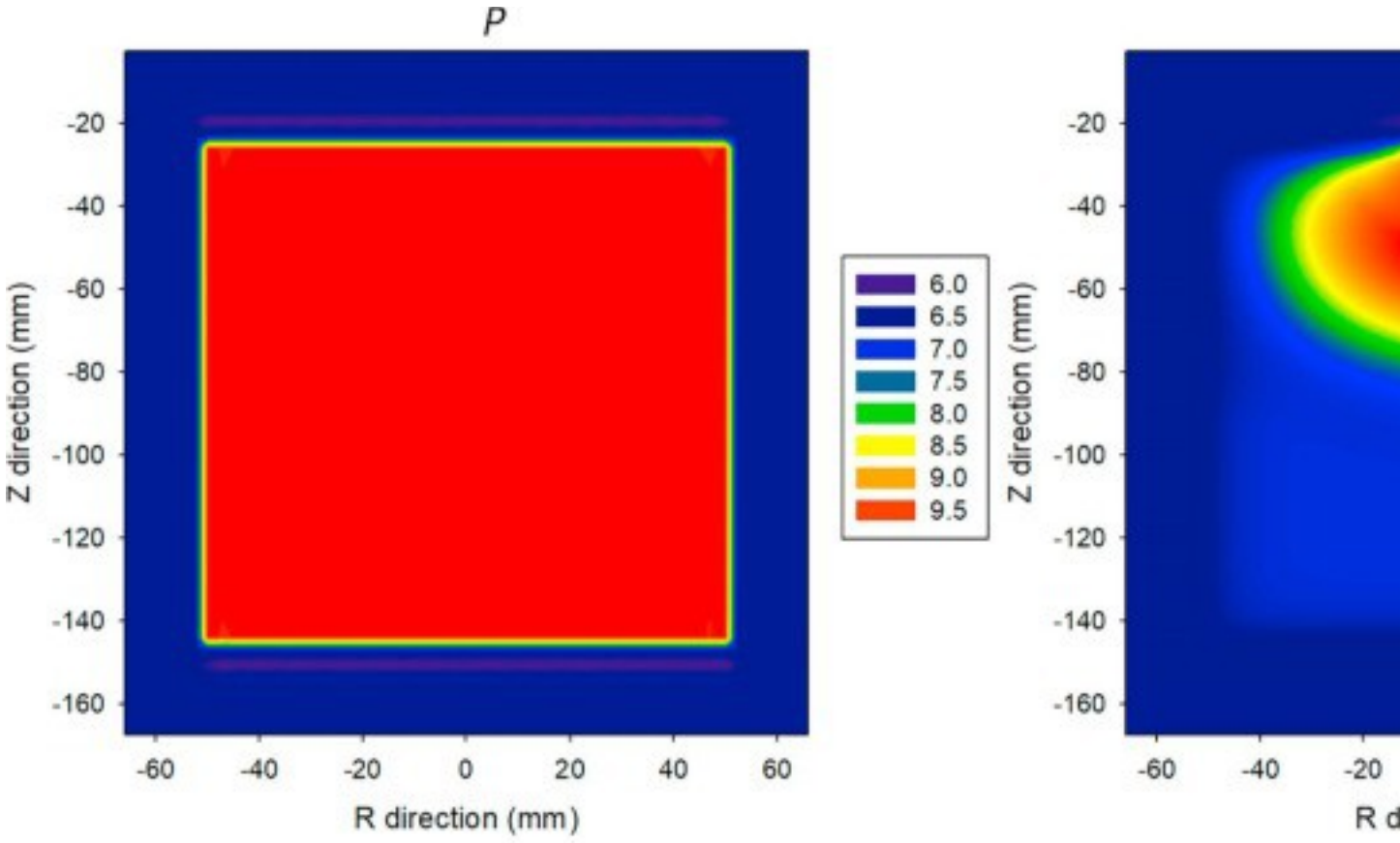
P
-20
-40
-60
-80
-100
-120
-140
-160
Z direction (mm)
-60
-40
-20
0
20
40
60
R direction (mm)
6.0
6.5
7.0
7.5
8.0
8.5
9.0
9.5

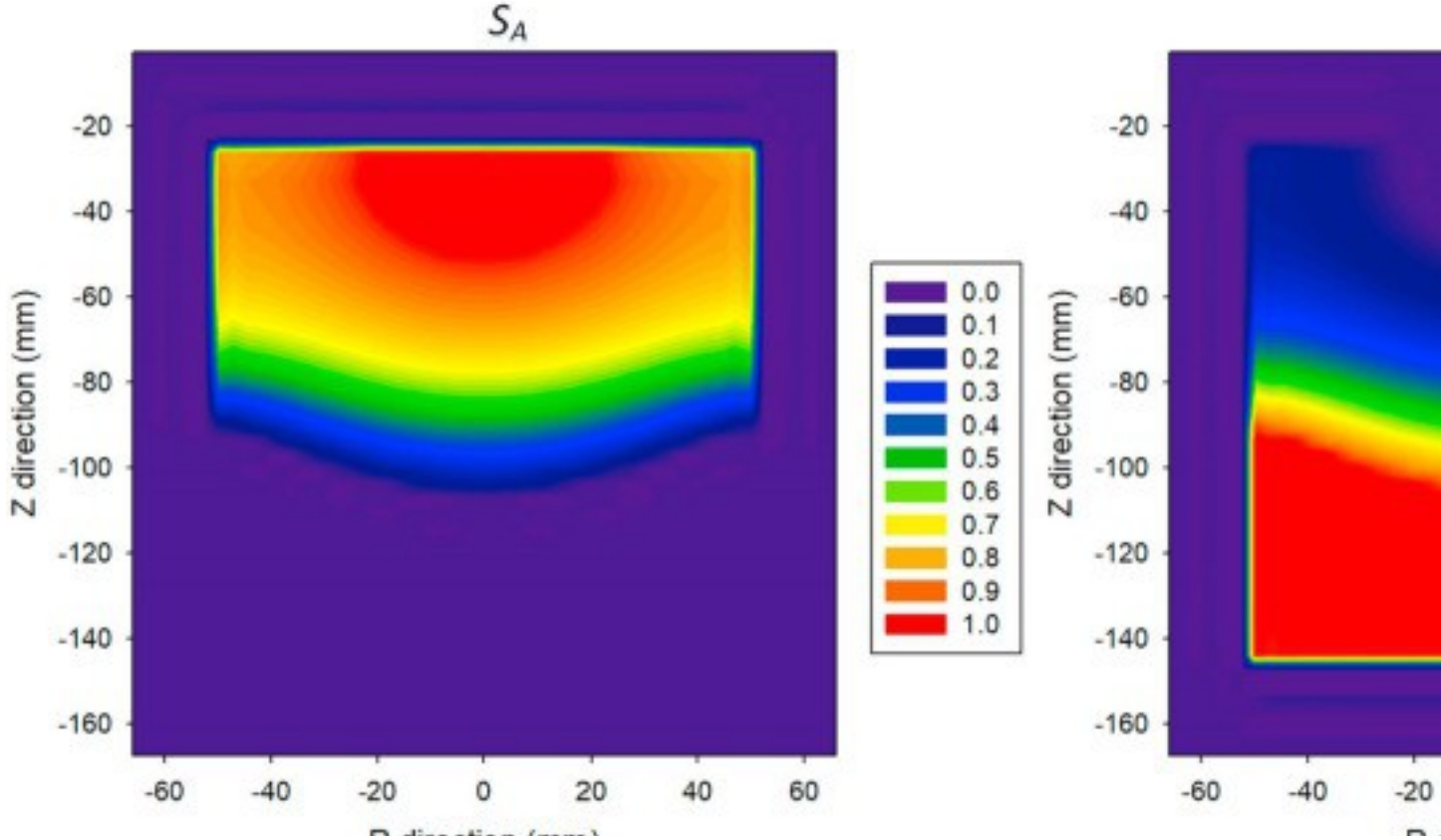
S_A
-20
-40
-60
-80
-100
-120
-140
-160
Z direction (mm)
-60
-40
-20
0
20
40
60
0.0
0.1
0.2
0.3
0.4
0.5
0.6
0.7
0.8
0.9
1.0

1. Download high-res image (268KB)
2. Download full-size image

Fig. 8. Spatial distribution of P, T, S_A, and S_G at the end of Step I1.

4.2. Step S1: 1st stabilization

The 2.0 h-long Step S1 was designed to allow phase redistribution and homogenization (to the extent possible) of S_A and S_G in the reactor. Fig. 9 shows a very good agreement between the observed and the numerically predicted P and T. The estimated $C_R = 1309$ J/kg/K appears somewhat elevated compared to values reported in the literature (around 812 J/kg/K [111]), but it is deemed as reasonable given the low-level compaction of the sand in the reactor (as indicated by the high ϕ), which indicates limited grain-to-grain contact and thus higher energy requirement in order to effect an increase in the sand temperature. The estimated $k_{\theta w} = 2.5$ W/m/K is well within the range of quartz sand with a $\phi = 0.448$ [112], [113]. Given the limited processes involved in the study of Step S1, we are confident that the estimates of $k_{\theta w}$ and C_R are reliable.

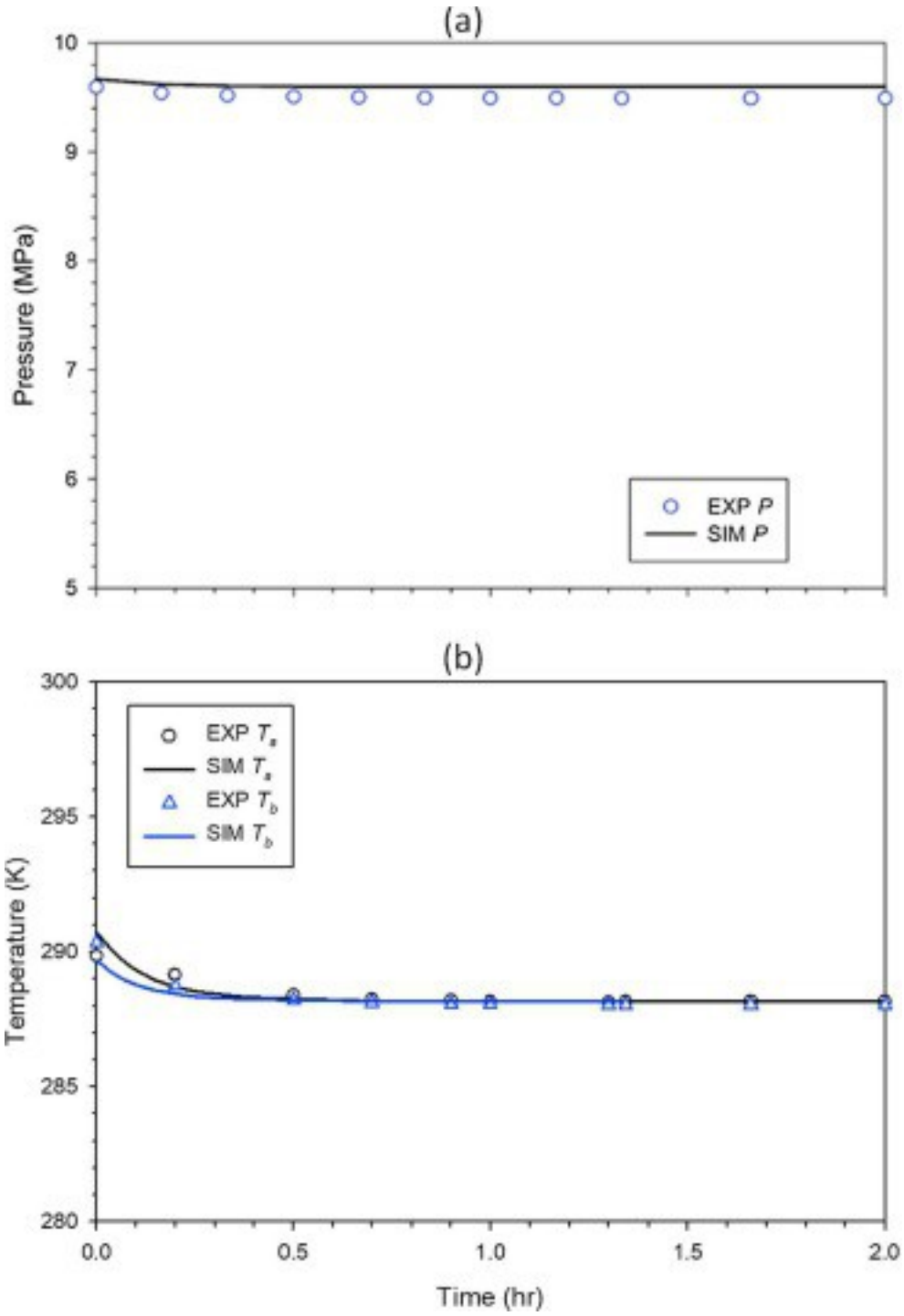

1. Download high-res image (86KB)
2. Download full-size image

Fig. 9. (a) Evolution of *P* over time during Step S1. (b) Evolution of temperature at T_a and T_b over time during Step S1.

The small but consistent *P*-deviations of about 1% between the two sets are attributed to measurement imperfections and errors during the manual operation of the system

valves. The small decrease in P that is observed early in Step S1 is attributed to (a) gas dissolution, as the injected CH_4-free water drains toward the bottom of the reactor and comes in contact with the CH_4 gas there, in addition to (b) the decrease in temperature caused by the constant-T boundary.

Fig. 10 shows the spatial distribution of P, T, S_A and S_G at the end of Step S1. For the reasons discussed in the previous Section 4.1, P is practically uniform within the reactor. The temperature T is now uniformly distributed because sufficient time has passed for the circulating heat-exchange fluid to effect a steady state. Of particular interest are the S_A and S_G distributions, which are clearly heterogeneous because the high permeability of the porous medium and its low irreducible water saturation $S_{irA} = 0.12$ (see Table 4) leads to drainage of water and its accumulation at the bottom of the reactor where $S_A = 60\%$, while S_A is only about 30% near the top of the reactor. This is an early indication that the general assumption of a uniform hydrate distribution in experimental studies involving laboratory-made hydrates (formed following standard practices) is invalid even in small reactors.

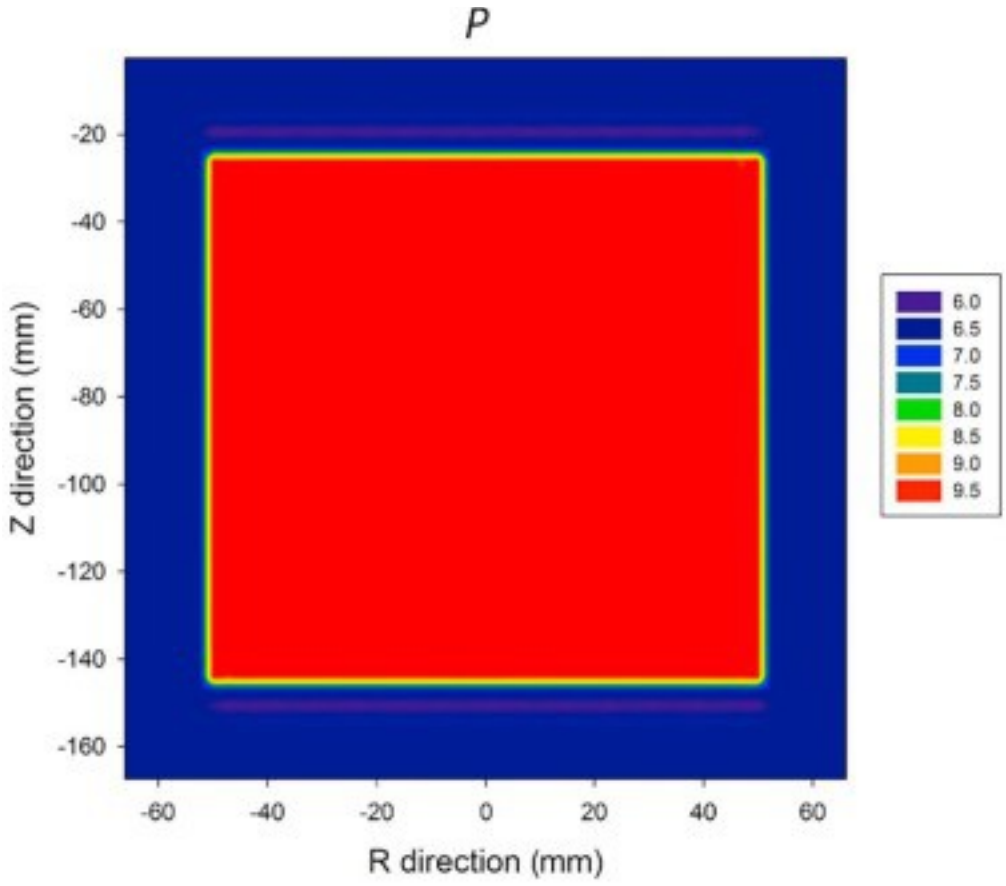
P
-20
-40
-60
-80
-100
-120
-140
-160
Z direction (mm)
-60
-40
-20
0
20
40
60
R direction (mm)
6.0
6.5
7.0
7.5
8.0
8.5
9.0
9.5

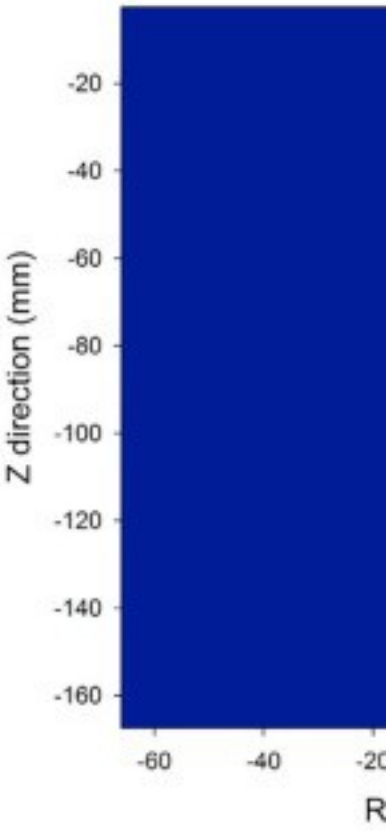
-20
-40
-60
-80
-100
-120
-140
-160
Z direction (mm)
-60
-40
-20
R

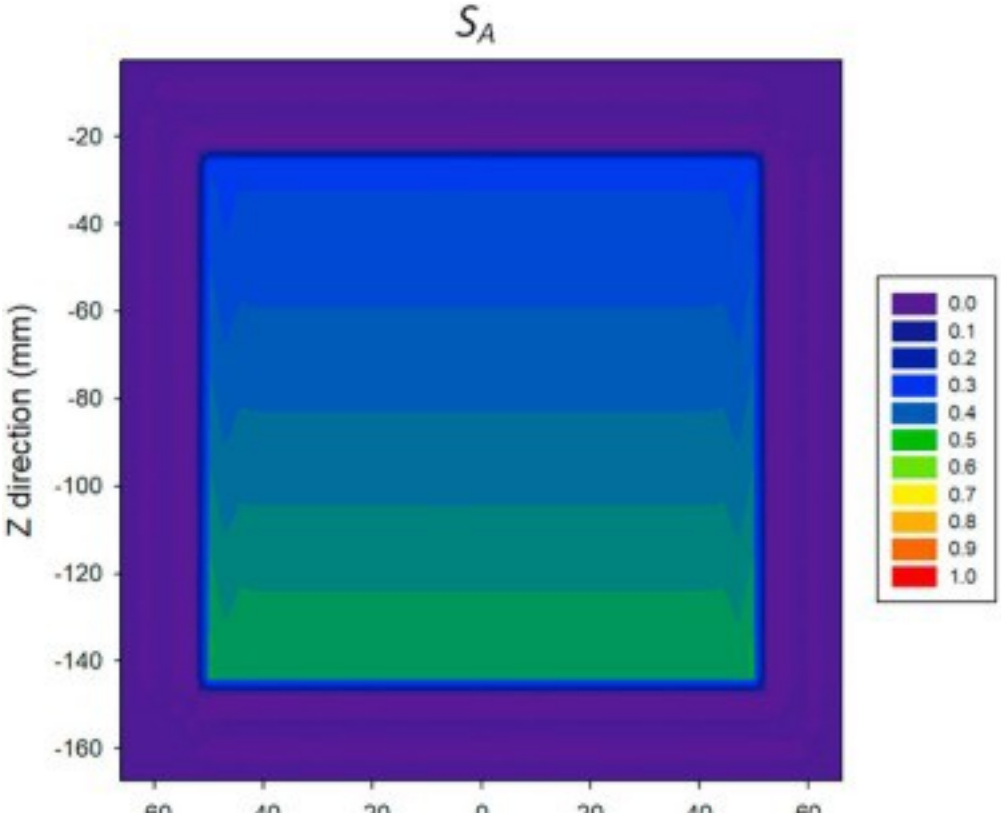
S_A
-20
-40
-60
-80
-100
-120
-140
-160
Z direction (mm)
0.0
0.1
0.2
0.3
0.4
0.5
0.6
0.7
0.8
0.9
1.0

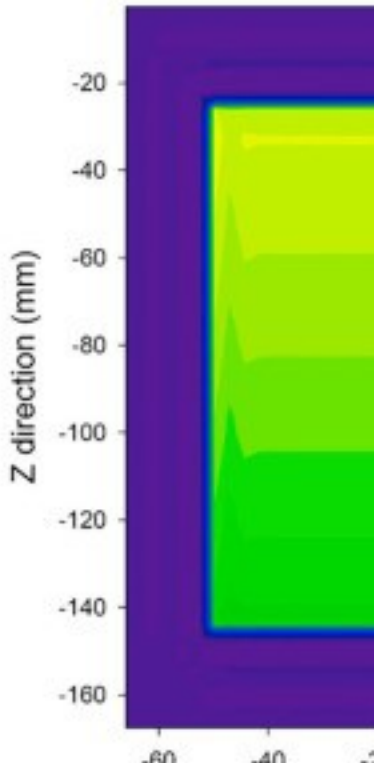
-20
-40
-60
-80
-100
-120
-140
-160
Z direction (mm)

1. Download high-res image (193KB)
2. Download full-size image

Fig. 10. Spatial distribution of P, T, S_A, and S_G at the end of Step S1.

4.3. Step F1: Cooling and 1st hydrate formation

4.3.1. Equilibrium vs. kinetic hydration reaction

In order to determine whether the formation process is best described by an equilibrium or a kinetic reaction, two sets of simulation were conducted for the analysis of Step F1, during which hydrate formation first occurs in response to a reduction in the temperature of the heat-exchange fluid (see Table 2 and Fig. 5b). The initial conditions are those at the end of Step S1, and all relevant conditions and thermophysical parameters were as listed in Table 4.

The experimental observations in Fig. 11a show that P in the reactor decreased continuously from 9.5 MPa to 3.2 MPa during Step F1 because of the consumption of the hydrate-forming CH_4, which easily outweighs the effect of the water consumption (the density of the CH_4-hydrate is less than that of H_2O, thus hydrate formation tends to decrease pore free space and to lead to a higher P). The equilibrium simulations indicated a very fast hydrate formation, which was to be expected given the nature of such a reaction model. The rate of the reaction, as quantified by the reduction in P, could not be reconciled with the experimental data when the initial value of $k_{\theta w}$ was as listed in Table 6. Thus, several scoping calculations involving sensitivity analysis indicated that (a) the evolution of pressure was sensitive only to the value of $k_{\theta w}$ and the only way to delay the rate of the reaction was to reduce its value, (b) the hydrate formation under the conditions of the experiment was (i) a thermally-dominated process and (ii) practically insensitive to the flow parameters of the porous medium.

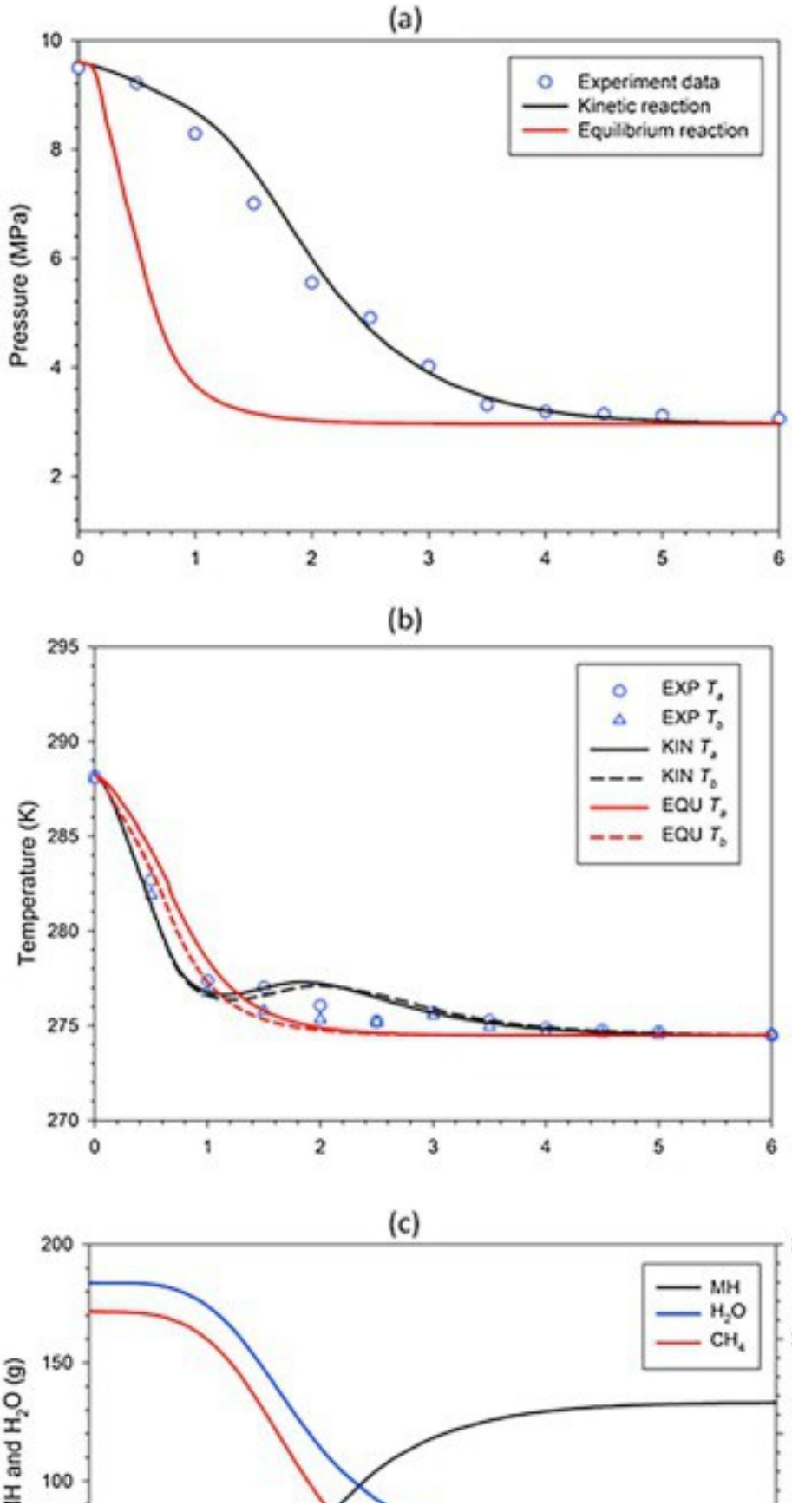
(a)
Experiment data
Kinetic reaction
Equilibrium reaction
Pressure (MPa)
(b)
EXP T_a
EXP T_b
KIN T_a
KIN T_b
EQU T_a
EQU T_b
Temperature (K)
(c)
MH
H_2O
CH_4
H and H_2O (g)
of CH_4 (g)

1. Download high-res image (129KB)
2. Download full-size image

Fig. 11. (a) Evolution of P over time during Step F1. (b) Evolution of T_a and T_b over time during Step F1. (Note that EXP = experiment data; KIN = kinetic reaction case; EQU = equilibrium reaction case) (c) Evolution of the mass of H_2O, CH_4 and MH phase during Step F1.

Table 6. Optimized thermophysical parameters used in each step.

Period	Step	ϕ	S_{irA}	$k_{\theta w}$(W/m/K)	C_R (J/kg/K)	N_H	F_A
	I1	0.448	0.12	1.65	1380	—	—
1st Period	S1	0.448	0.12	2.50	1309	—	—
	F1	0.448	0.12	2.50	1309	6.1	0.23
	I2	0.448	0.12	2.50	1309	6.1	35 ($t \le 60$ s) 3.2 (60 s $< t \le$ 120 s) 2.2 (120 s $< t \le$ 180 s) 0.01 (180 s $< t \le$ 250 s)
2nd Period	F2	0.448	0.12	2.50	1309	6.1	1.5×10^{-3} ($t <$ 2 h) 7.6×10^{-4} (2 h $< t \le$ 6 h) 2.5×10^{-4} (6 h $< t \le$ 24 h) 6.0×10^{-5} (24 h $< t \le$ 72 h)
3rd Period	I3	0.448	0.12	2.50	1309	6.0	1.0×10^{-6}
	F3	0.448	0.12	2.50	1309	6.0	1.0×10^{-6}

Fig. 11a shows a comparison of the experimental measurements of the evolution of P to the numerical predictions obtained using an equilibrium model of hydrate formation and a value of $k_{\theta w} = 0.5$ W/m/K. This $k_{\theta w}$ value is representative of an oven-dry sand and well below any value reported for a fully-saturated porous medium, and still results in a pressure drop (= reaction rate) that is significantly faster than the experimental evidence. Thus, it took less than 1.5 h to attain the stable final $P = 3.1$ MPa that indicated cessation of hydration even for this unnaturally low value of $k_{\theta w}$. The inevitable conclusion is that the hydrate formation reaction in the laboratory experiments of Chong et al. [51] cannot be represented by an equilibrium model.

Fig. 11a also shows the numerical predictions of the evolution of Pobtained using the optimized data values from the history-matching process for a kinetic hydration reaction.

This simulation used the optimized values of the other parameters that were determined in Steps I1 and S1 (see Table 6). The history-matching process in Step F1 involved concurrent use of both the P and T data and focused on the optimization of the F_A factor (see Section 3.4), which for the value of $F_A = 0.23$ matched the duration of the hydrate-forming process at about 4.5 h and yielded a very good agreement with the laboratory P-measurements (Fig. 11a). The deviations between observed and estimated pressures in Fig. 11a are attributed to measurement errors, imperfection in the estimation of the reaction surface area A, as well as in temporal variability in F_A (and its intertwined variable K_0) as P and T changed during Step F1.

Fig. 11b shows the experimental measurements and the numerical estimates (for both an equilibrium and a kinetic hydration reaction) of the evolution of the T over time. The experimental measurements (T_a and T_b) are averages of the measurements of the various thermocouples along the length of each of the two sensors lines at the locations a and b shown in Fig. 3. The corresponding numerical estimates are also averages of the T-predictions at the elements most closely corresponding to the thermocouple locations, and were obtained by using the parameter values from history-matching (against the combined P- and T-data sets) that also yielded the results in Fig. 11a. The agreement between observations and the numerical estimates from the kinetic model is good, capturing the precipitous initial drop caused by the initial rapid hydrate formation and the tail end at the later part of Step F1. The differences between the two from $t = 1.0$ h to $t = 3.0$ h correspond to an increase in temperature that appears to indicate a period during which the heat release caused by the exothermic hydrate formation exceeds the rate of heat removal by the circulating cooling heat exchange fluid. Both the experimental and the numerical data indicate such a “bump” in T, but these occur at different times and the T-increase is more pronounced in the numerical predictions. The maximum T-difference is less than 2 K, and the deviations are attributed to the following possible reasons: (a) mismatch of the locations of the sensors and of the centres of the grid elements in the simulations, given the very sharp saturation and T-fronts that are the norm in hydrate formation, (b) localized phase saturation heterogeneities that cannot be captured in the absence of visualization capabilities (temperature sensors respond not only to advective heat flows but also to conductive ones that are much more sensitive to localized heterogeneities), (c) the use of a hydrate $P_{eq} - T_{eq}$ relationship obtained from dissociation experiments, when there is evidence of a yet-unquantified “hysteretic” behaviour during hydrate formation [7], (d) possible imperfections of the HBS thermal conductivity model in capturing some relatively short-term processes (Table 4), and, last but not least, (e) limitations of the

kinetic model of Kim et al. [50] and Clarke and Bishnoi [114], which was developed from dissociation (not formation) data and for conditions that are not representative of hydrates in porous media.

The numerical predictions of T_a and T_b for the equilibrium model (shown for completeness in Fig. 11b) are consistently higher than those for the kinetic model during hydrate formation. This was expected because the much faster hydrate formation rate (an exothermic reaction) under equilibrium conditions leads to faster release of heat and, consequently, to higher *T*-estimates.

The laboratory *P*- and *T*-data clearly showed a kinetic retardation that could not be reconciled with any combination of reasonable variable values in an equilibrium hydration model, but which was easily and accurately captured when using a kinetic model. These results confirm the earlier conclusion of Kowalsky and Moridis [94]that a kinetic model is recommended in the description of short-term processes lasting a few hours to a few days, as is the case of most laboratory experiments. Thus, all subsequent steps in Periods 2 and 3 of this study were analysed using a kinetic model.

4.3.2. Spatial distributions of *P*, *T*, S_H, S_A and S_G

Fig. 12 shows the evolution of spatial distribution of *P*, *T,* S_H, $S_A$and S_G at specific times during the Step F1. The high permeability and porosity of the sand result in the practically uniform P-distribution in the reactor at all times (Fig. 12a). The formation of hydrates leads to the heterogeneous *T*-distribution at early times, but cessation of hydration and the continuous effect of the cooling boundaries (in addition to the very high thermal conductivity of the reactor metal) leads to a practically uniform *T*-distribution at $t > 4.5$ h (Fig. 12b).

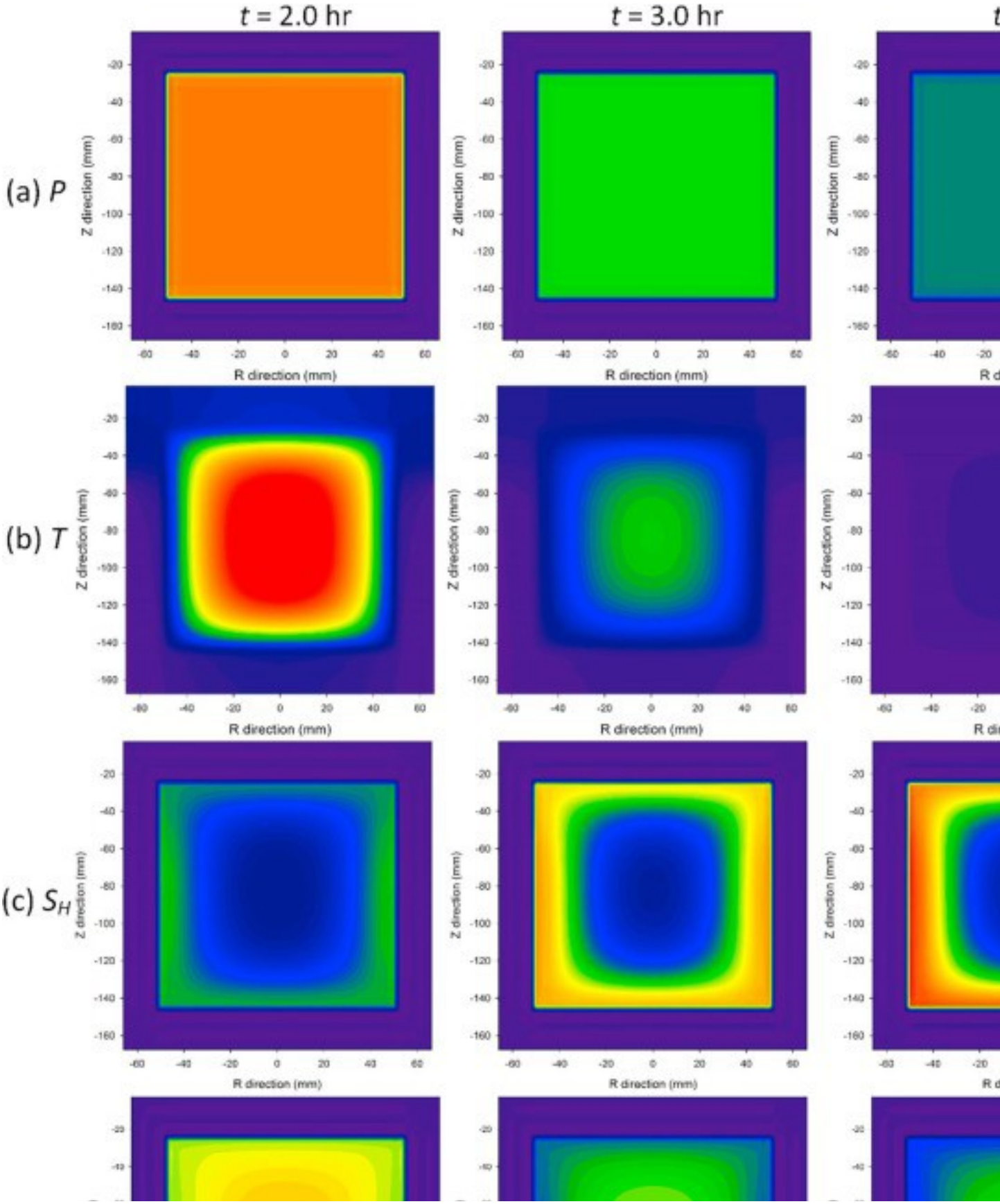
t = 2.0 hr
t = 3.0 hr
(a) P
(b) T
(c) S_H
Z direction (mm)
R direction (mm)
-20
-40
-60
-80
-100
-120
-140
-160
-60
-40
-20
0
20
40
60

1. Download high-res image (427KB)
2. Download full-size image

Fig. 12. Evolution of spatial distribution of P, T, S_H, S_A, and S_G over time during Step F1. Note that there are no changes in the phase saturations for $t > 5.0$ h.

Changes in the phase saturations cease for $t > 5.0$ h. The distribution of the phases saturations are heterogeneous (and significantly so) in all cases and at all times along both the r- and the z-axes, and undermines the validity of the frequent assumption of uniform distribution in the analysis of laboratory experiments [47], [65], [87], [89], [115]. Thus, S_H (a) increases in the entire domain as time advances, (b) is at its maximum along the areas of contact with the cooling heat-exchange fluid (located in the lower part of the reactor, see Fig. 3), and (c) decreases toward the interior/centre of the reactor. At the end of Step F1, $S_H = 0.49$ next to the cooling boundary, but it is only $S_H = 0.10$ at the centre of the reactor. The steep S_H fronts at the locations of the sensors (Fig. 3, Fig. 12c) and the associated steep T-fronts during hydrate formation further support the explanation for the deviations between observations and simulation results discussed in Fig. 11.

Because hydrate formation resulted in consumption of CH_4 and H_2O, the S_A and S_G distributions followed a pattern that was the opposite of that of S_H. Thus, the lowest saturations were observed along the areas of contact with the cooling heat-exchange fluid, and the highest ones (e.g., $S_G > 0.60$) at and near the centre of the reactor where hydrate formation had been limited. Fig. 11c presents the evolution of the mass of H_2O, CH_4 and MH phase during Step F1, again confirming that MH formation starts slowly within the first 1.0 h of cooling, then grows rapidly during the period of 1.0–3.0 h and stops practically after $t > 5.0$ h. In addition, the formation of MH results in a consumption of both H_2O and CH_4 with a decreasing trend that mirrors the MH formation.

4.4. Step I2: 2nd water injection

Fig. 13a shows an excellent agreement between the observed evolution of P during Step I2 and the numerically predictions obtained using the optimized parameters (see Table 6). During this water injection step, P continuously increased from 3.2 MPa to 9.6 MPa. The T_a and T_b observations and the predictions at the same locations (Fig. 13b) capture (a) the same general spatial effects, with the locations further from the injection point showing a lower T-increase, and (b) the same upward trend over time, which was caused by several reasons: gas compression, injection of warm water, and the exothermic reaction of hydrate formation near the reactor centre in response to the increasing P. Their agreement is initially good (especially in the case of T_b), but some

deviations occur. These are attributed mainly to intense localized heterogeneities, associated with the very steep phase saturation fronts that occur when the injected warm water comes in contact with the hydrate formed in Step F1, as well as all other reasons discussed in Section 4.3.1. This appears to be supported by Fig. 13b, which shows the T_b sensors experiencing an initial T-increase larger in magnitude and earlier than the T_a ones despite being further from the injection point. These initial "anomalous" T-responses are alleviated over time as more water is injected, and the sensors closer to the injection point eventually register higher temperatures at the end of Step I2.

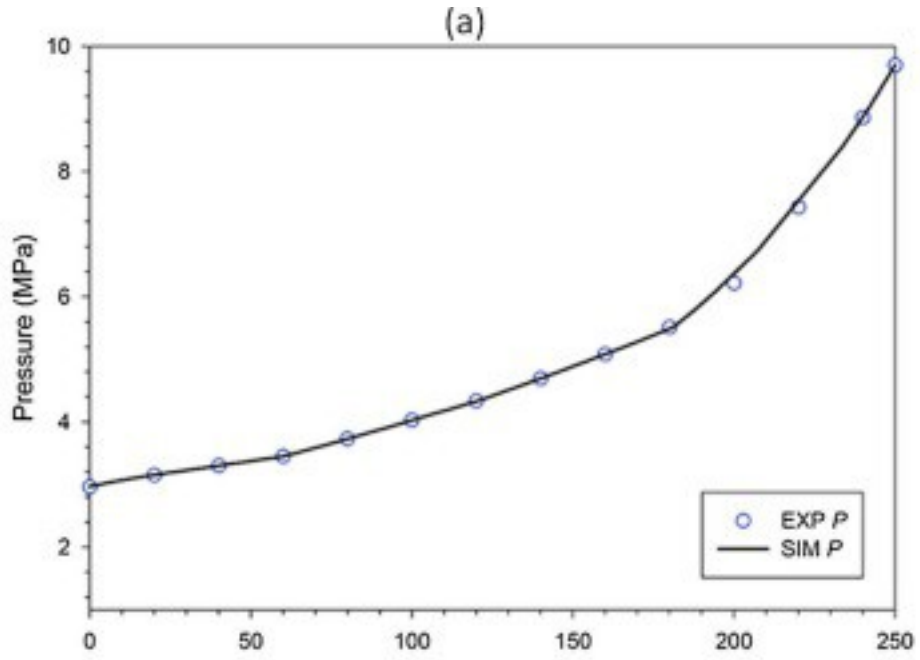
(a)
Pressure (MPa)
EXP P
SIM P

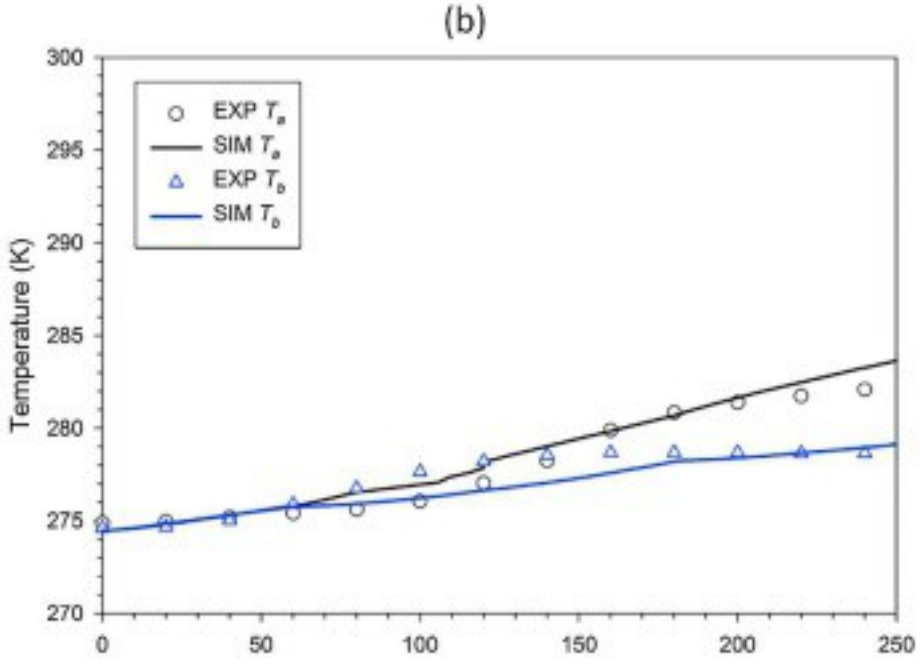
(b)
Temperature (K)
EXP T_a
SIM T_a
EXP T_b
SIM T_b

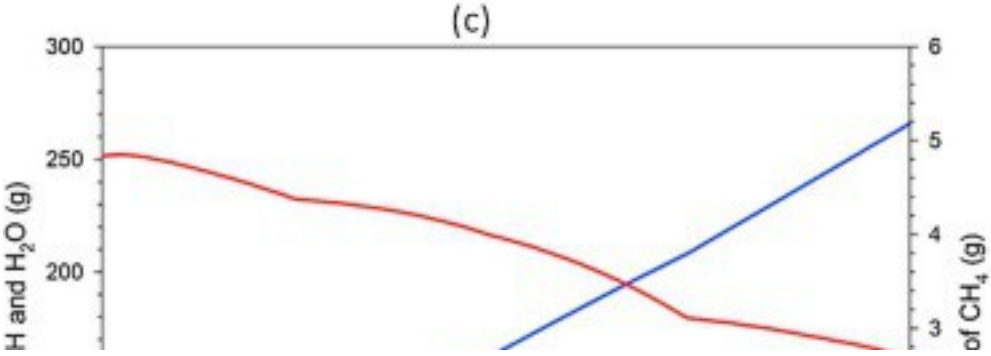
(c)
H and H_2O (g)
of CH_4 (g)

1. Download high-res image (124KB)
2. Download full-size image

Fig. 13. (a) Evolution of P over time during Step I2. (b) Evolution of T over time during Step I2. (c) Evolution of the mass of H_2O, CH_4 and MH phase over time during Step I2.

The spatial distributions of P, T, S_H, S_A and S_G in Fig. 14 reveal the complicated processes that occur during Step I2. These involve hydrate dissociation caused by the "thermal shock" of the warm water coming in contact hydrate, as well as hydrate formation elsewhere in the reactor (at locations unaffected by the invading warm water but experiencing the P-increase). For reasons already explained, P in the reactor remains spatially uniform at all times during Step I2, and its level increases with time as incompressible H_2O is injected (Fig. 14a). The non-uniform T distribution in Fig. 14b shows clearly the effect of the injected and invading warm water (see Fig. 14d), the footprint of which expands over time. The S_H distribution in Fig. 14c shows (a) complete hydrate dissociation at locations that correspond very closely to those exhibiting higher T in Fig. 14b, but also (b) continuous hydrate formation (caused by the rising P) along the outer surfaces of the sand body that are unaffected by the injected warm water (mainly along the contact areas with the cooling fluid and near the reactor bottom).

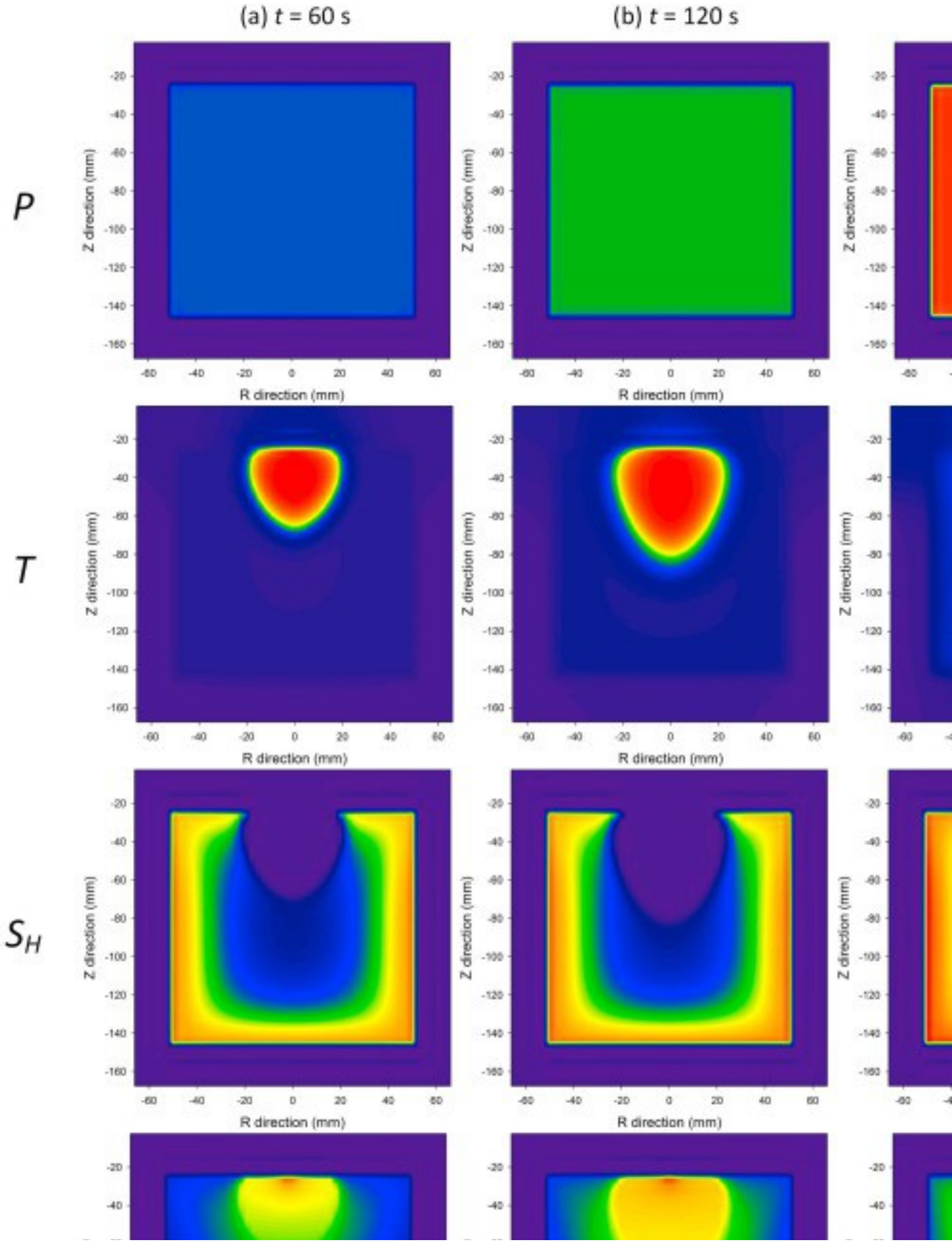
(a) t = 60 s
(b) t = 120 s
P
T
S_H
Z direction (mm)
R direction (mm)

1. Download high-res image (957KB)
2. Download full-size image

Fig. 14. Evolution of spatial distribution of P, T, S_H, S_A, and S_G over time during Step I2. (left S_G scale for $t = 60$ s and 120 s; right S_G scale for $t = 250$ s)

The spatial distribution of S_G in Fig. 14e shows the most complex pattern, which is the combined result of (a) the gas release associated with the hydrate dissociation caused by the injected warm water, (b) the compression of the free gas in the reactor at the beginning of Step I2, and (c) the gas consumption associated with the hydrate formation discussed earlier. The evolution of the mass of free CH_4 gas, H_2O and CH_4-hydrate phase shown in Fig. 13c provides an important insight into the relative importance of the dissociation vs. formation process. Thus, the warmer H_2O injection appears to cause a short-term (about 10 s) hydrate dissociation that is indicated by and almost imperceptible drop in the MH mass and a similarly small increase in the mass of free CH_4 gas. However, hydrate formation is clearly dominant for the rest of Step I2, as is indicated by the monotonically increasing MH mass and the correspondingly decrease of the free CH_4 gas. This means that, with the exception of a very short initial time, the monotonic and continuous increase in pressure caused by the H_2O injection leads to hydrate formation (at locations unaffected by the invading warm H_2O) that exceed the hydrate dissociation induced by the warm water near the injection point. Note that the mass of H_2O increases continuously during Step I2 because its injection rate exceeds at all times its consumption for the MH formation.

4.5. Step F2: 2nd hydrate formation

Fig. 15a and b shows a very good agreement between the numerically predicted and the observed P and T during the 72.0 h of hydrate formation in Step F2. The initial steep decline in P during the first 6.0 h was followed by a progressively milder decline. The pattern of pressure declines was associated with the corresponding rates of hydrate formation (as well as CH_4 and H_2O consumption, see Fig. 15c), and was also reflected in the values of F_A that indicated a continuously decelerating reaction (see Table 6 and Fig. 16). Additional reasons for the pressure decline included cooling (that affected significantly the gas pressure), as well as dissolution of CH_4 into the injected water that is enhanced as cooling continues. The cooling of the interior of the reactor is evident in the evolution of T_a and T_b in Fig. 15b, which exhibit a fast initial decline that is milder than that of pressure in Fig. 15a.

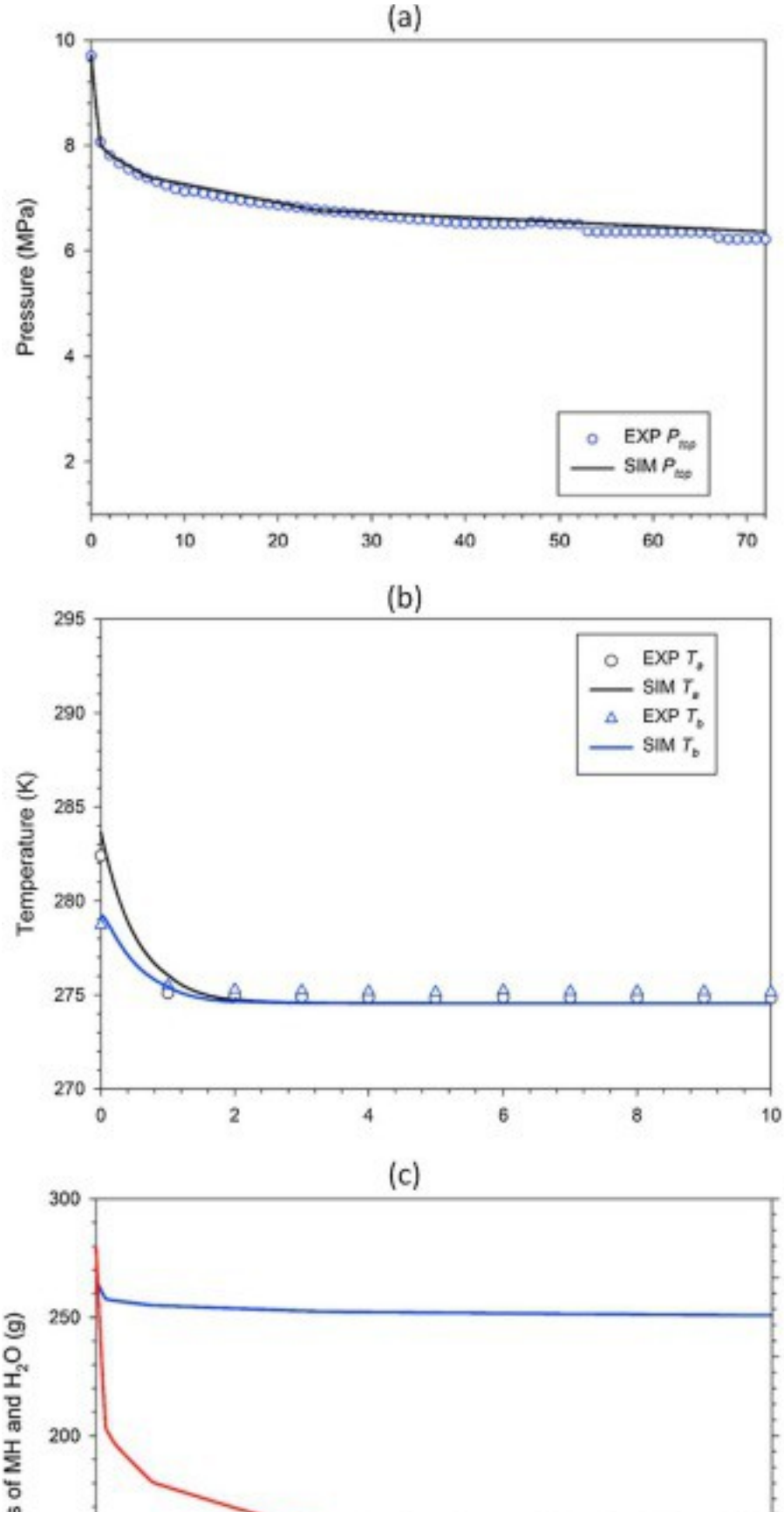
(a)
Pressure (MPa)
EXP P_{top}
SIM P_{top}
(b)
Temperature (K)
EXP T_a
SIM T_a
EXP T_b
SIM T_b
(c)
of MH and H_2O (g)
Mass of CH_4 (g)

1. Download high-res image (115KB)
2. Download full-size image

Fig. 15. (a) Evolution of *P* over time during Step F2. (b) Evolution of *T* over time during Step F2. (c) Evolution of the mass of H_2O, CH_4 and MH phase during Step F2.

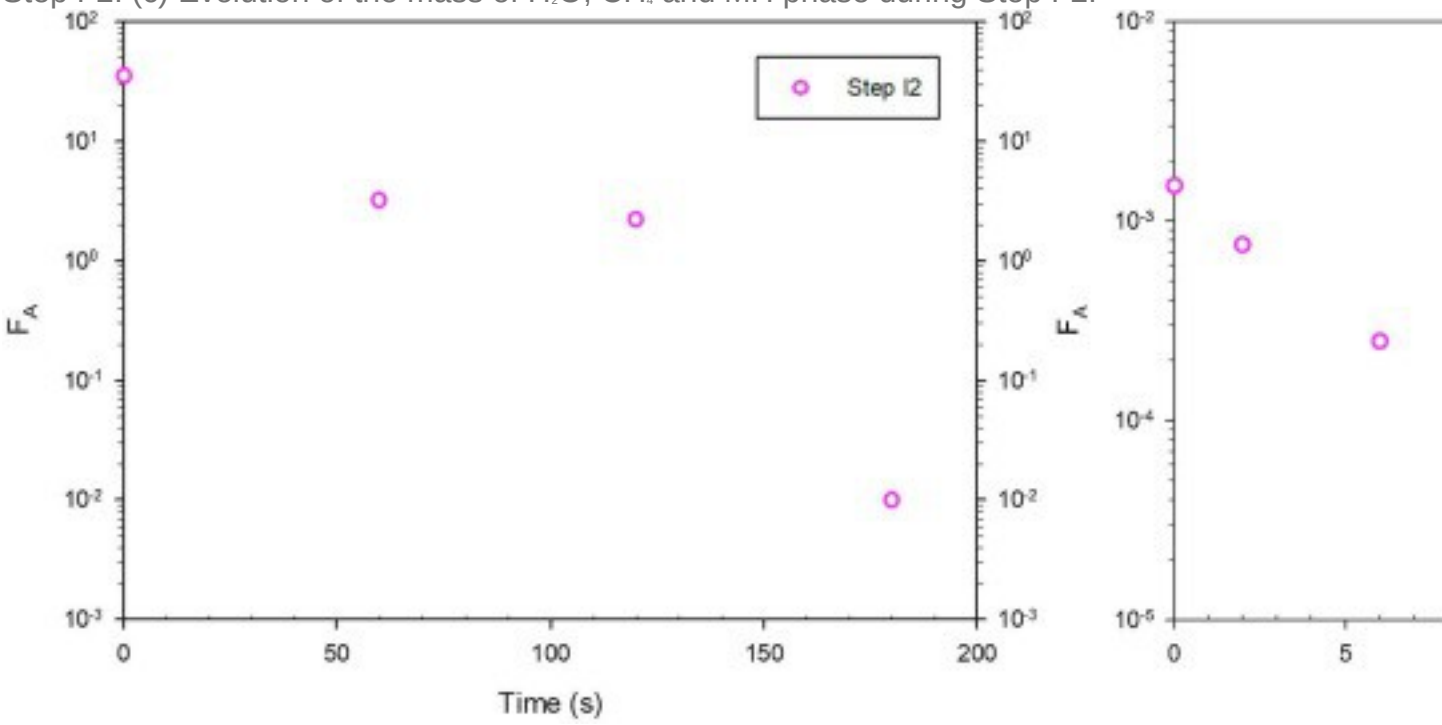

1. Download high-res image (79KB)
2. Download full-size image

Fig. 16. Summary of optimized surface adjustment factor (F_A) during Steps I2 and F2.

Of particular interest is the changing value of F_A (Fig. 16), which shows significant variability over the course of Steps I2 and F2. The value of $F_A = 35$ at the beginning of Step I2 indicates a very fast reaction that is probably approaching an equilibrium (as opposed to kinetic) reaction behaviour. The value of F_A declines rapidly from its initial value during both Steps I2 and F2. Note that F_A is an adjustment factor of the reaction area that describes the "cumulative" kinetic behaviour because it cannot be easily differentiated from the effects of the intrinsic rate constant K_0. The variability of F_A is attributed to several reasons: reduction in the surface area that participates in the hydrate formation reaction as the driving force for the reaction (i.e., the fugacity difference, see Table 5) is attenuated, imperfections in the underlying model of Moridis [93] that estimates the reaction surface area, and limitations of the underlying kinetic model of Kim et al. [50] and Clarke and Bishnoi [110], which was developed from hydrate formation data and under conditions that are markedly different from those encountered during hydrate formation in porous media. Thus, there is a possibility that

the kinetic reaction involves n^{th} powers of the fugacities or their difference (as opposed to their linear combinations), as well as a possibility that hydrate formation becomes dominated by diffusion processes (not captured by the current kinetic model) when the driving force becomes very mild as equilibrium is approached and CH_4 is nearly exhausted. Thus, an obvious recommendation of this study is to design appropriate laboratory experiments to address and elucidate these issues.

The spatial distributions of *P* in Fig. 17a shows the same pattern of uniformity encountered in all previous steps for the reasons already discussed. The *T*-distributions in Fig. 17b show that the intense *T*- differences shown in Step I2 (Fig. 14b) are attenuated over time and a near-uniform *T* is reached at the end of Step F2. It is difficult to visually discern significant changes in the distributions of S_H and S_A in Fig. 17c and d, respectively, which remain heterogeneous and quite close in appearance to those at the end of Step I2 (Fig. 14c and d). Note that at the end of Step F2, S_H reaches a maximum level of 63% along the inner surface of the reactor near the cooling system, while the minimum S_H in the reactor is only 2%. The changes in S_H and S_A can be better inferred from the S_G changes over time in Fig. 17e, which shows a continuous decrease in the amount of free gas that corresponds to additional (albeit limited) hydrate formation. This is confirmed quantitatively by the evolution of the CH_4 mass in Fig. 15c, which declines rapidly because of hydrate formation in a pattern that mirrors the pressure decline in Fig. 15a. The hydrate formation is further confirmed by the increase in the MH mass in Fig. 15c, as well as by the corresponding H_2O reduction.

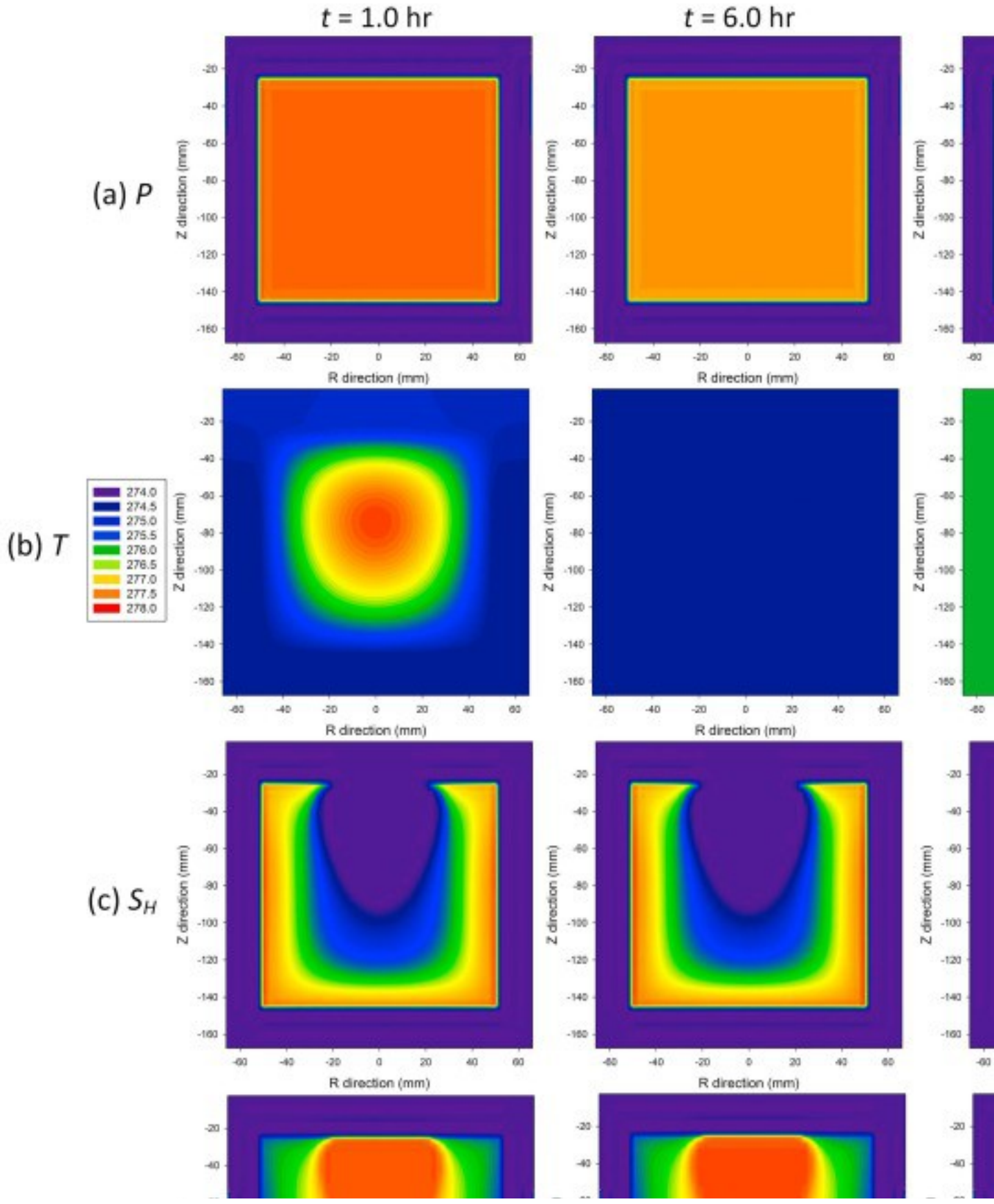
t = 1.0 hr
t = 6.0 hr
(a) P
(b) T
(c) S_H
274.0
274.5
275.0
275.5
276.0
276.5
277.0
277.5
278.0
Z direction (mm)
R direction (mm)

1. Download high-res image (970KB)
2. Download full-size image

Fig. 17. Evolution of spatial distribution of P, T, S_H, S_A, and S_G over time during Step F2. (left T scale for $t = 1.0$ h and 6.0 h; right T scale for $t = 72.0$ h)

4.6. Step I3: 3rd water injection

Fig. 18a and 18b shows an excellent agreement between the numerically predicted and the experimentally observed P and Tduring the 44 s of water injection in Step I3. The spatial distribution of P after Step I3 (Fig. 19a) at the end of the injection is again uniform for reasons already discussed. At the same time, T in Fig. 19b is highest near the injection nozzle, and a large part of the reactor volume appears unaffected by the limited amount of the injected warm water. Comparison of the S_A distribution at the end of Step I3 (Fig. 19d) to that at the end of Step F3 (Fig. 17d) shows the same pattern of spatial distribution but with a very slight expansion that is caused by the limited water injection. The $S_G$distribution in Fig. 19e shows the effect of water injection: a general reduction in the S_G magnitude compared to that in Fig. 17e, and a region in the vicinity of the nozzle where S_G is zero or negligible that clearly identifies the injected water (not discernible in Fig. 19d). The S_H pattern and magnitude in Fig. 19c are similar to those in Fig. 17c, indicating that the water injection did not lead to any significant hydrate dissociation. This is attributed to both the limited amount of injected water and to the shape of the S_H distribution already developed at the end of Step F2, which featured a near-hydrate-free region at the reactor centre near the injector, where the injected water is located (Fig. 19d). It is also confirmed by a constant mass of hydrate at 161.7 g with no additional hydrate formation during Step I3 shown in Fig. 18c, while the mass of H_2O phase increases because of water injection and the (already small) mass of CH_4 phase decreases because of the continuous dissolution into the injected water.

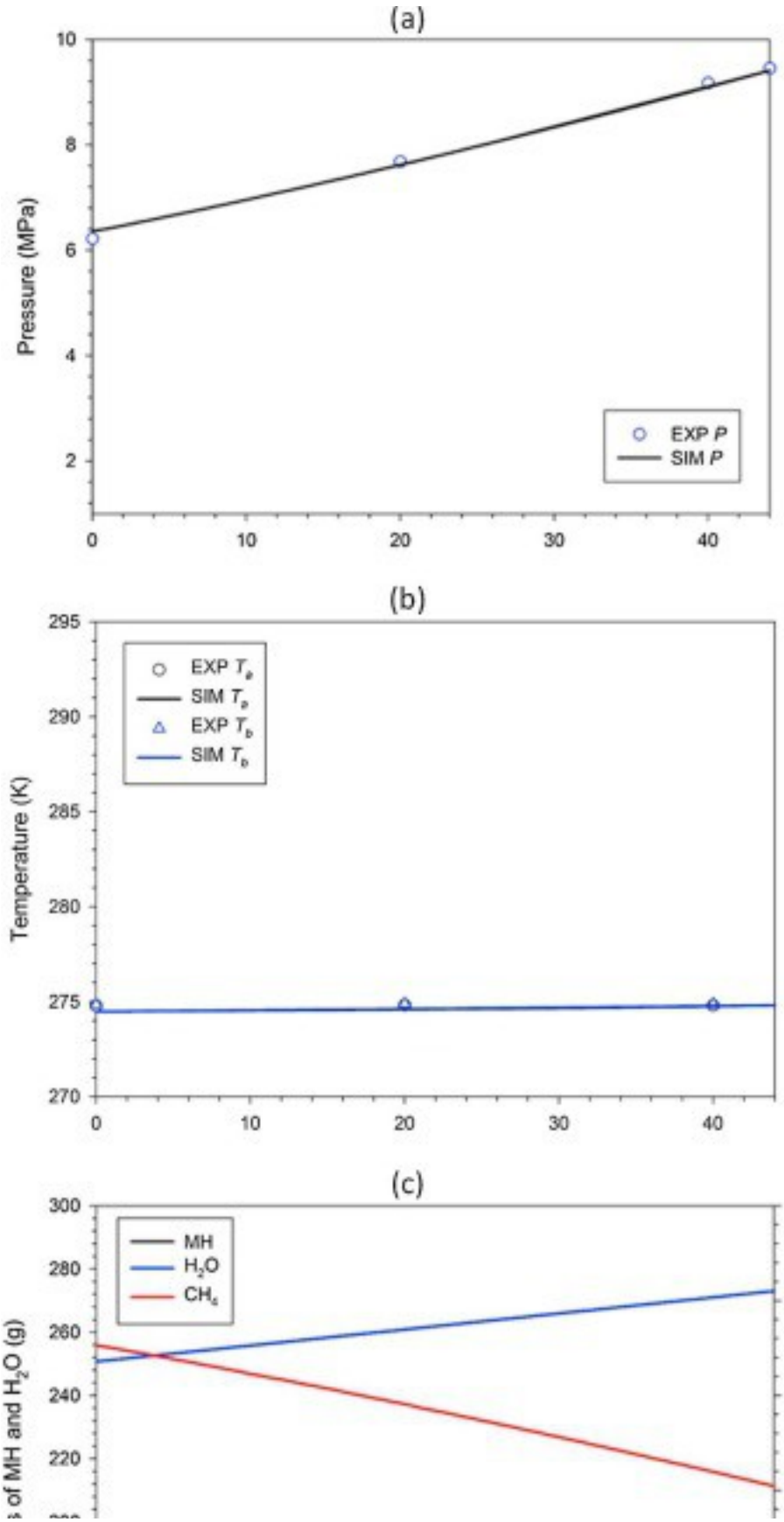
(a)
Pressure (MPa)
EXP P
SIM P
(b)
Temperature (K)
EXP T_g
SIM T_g
EXP T_b
SIM T_b
(c)
MH
H_2O
CH_4
Mass of MH and H_2O (g)
Mass of CH_4 (g)

1. Download high-res image (100KB)
2. Download full-size image

Fig. 18. (a) Evolution of *P* over time during Step I3. (b) Evolution of *T* over time during Step I3. (c) Evolution of the mass of H_2O, CH_4 and MH phase during Step I3.

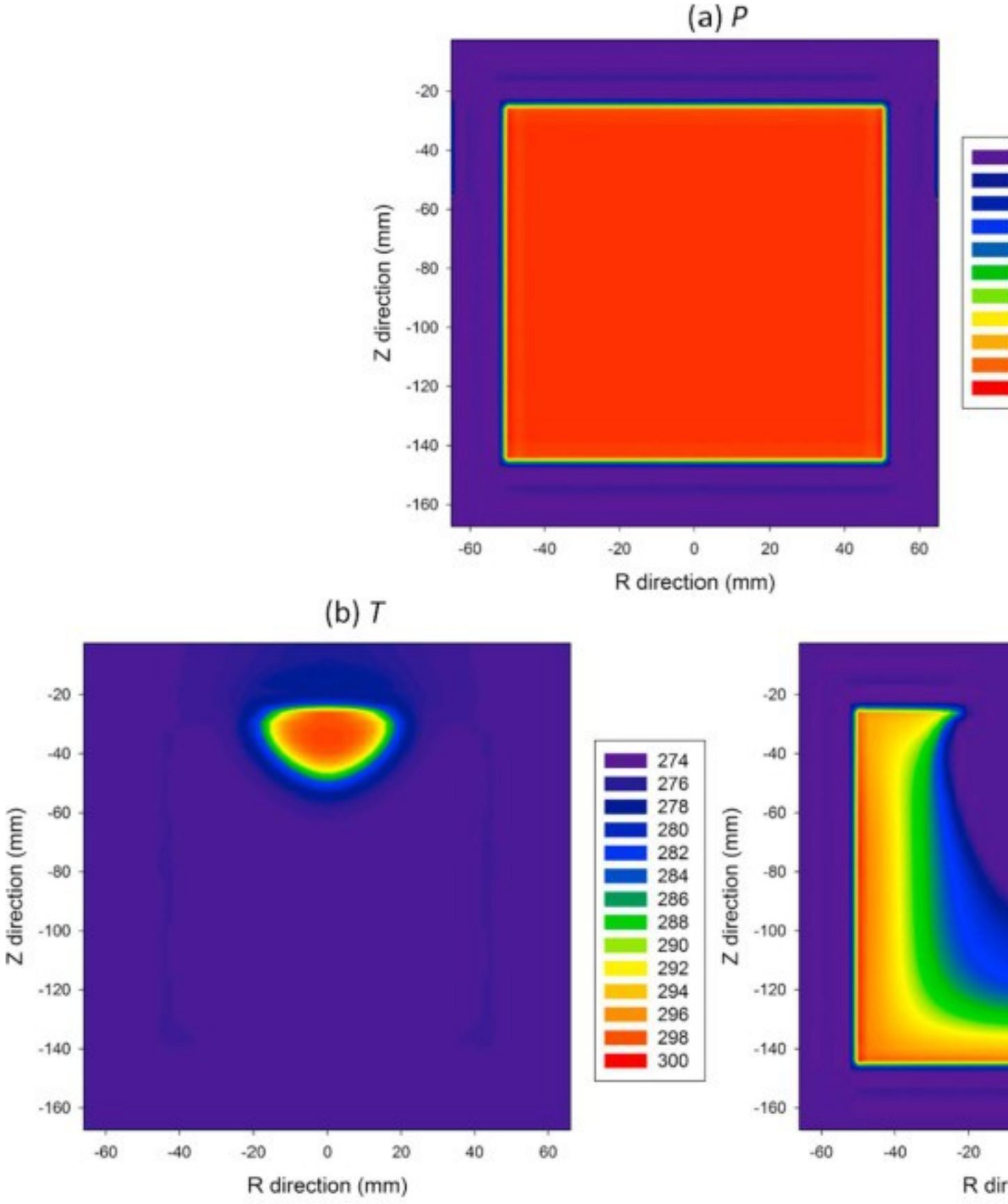
(a) P
Z direction (mm)
-20
-40
-60
-80
-100
-120
-140
-160
-60
-40
-20
0
20
40
60
R direction (mm)
(b) T
Z direction (mm)
R direction (mm)
274
276
278
280
282
284
286
288
290
292
294
296
298
300

1. Download high-res image (304KB)
2. Download full-size image

Fig. 19. Spatial distribution of P, T, S_H, S_A, and S_G at the end of Step I3.

4.7. Step F3: 3rd hydrate formation

Fig. 20a and 20b shows an excellent agreement between the numerically predicted and the observed P and T during the 72.0 h of hydrate formation in Step F3. P decreased from 9.47 MPa to 8.72 MPa, while T remains practically constant at 274.4 K after an initial short-term decline from 274.8 K. Note that F_A appears to be constant during Steps I3 and F3 (Table 6), possibly because of the mild-long term processes attributed (a) the limited amounts of the injected H_2O and (b) available CH_4, as well as (c) the shape of the body of the hydrate and the associated S_H heterogeneity.

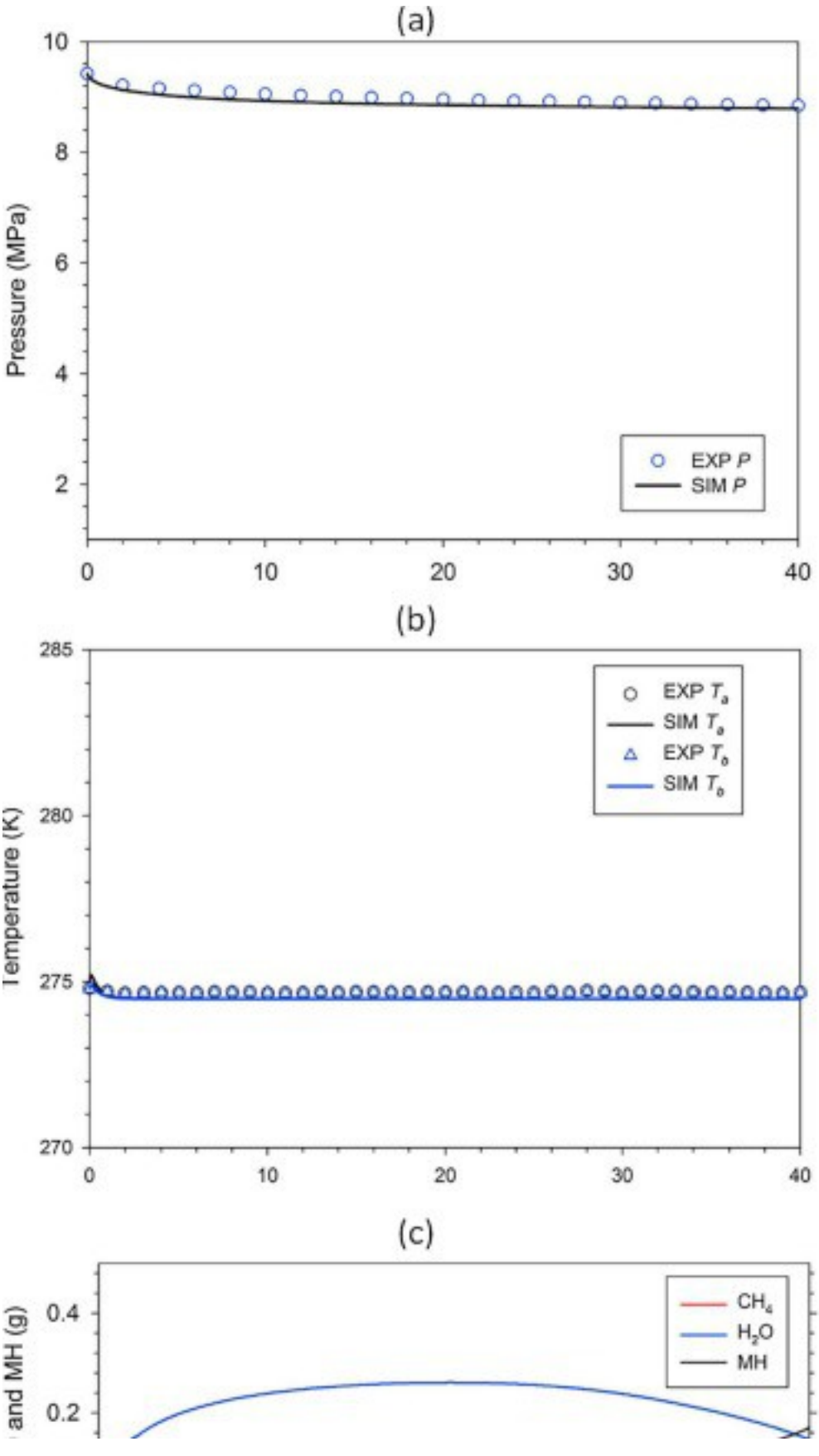
(a)
Pressure (MPa)
10
8
6
4
2
0
10
20
30
40
EXP P
SIM P
(b)
Temperature (K)
285
280
275
270
0
10
20
30
40
EXP T_a
SIM T_a
EXP T_o
SIM T_o
(c)
and MH (g)
0.4
0.2
CH_4
H_2O
MH

1. Download high-res image (120KB)
2. Download full-size image

Fig. 20. (a) Evolution of P over time during Step F3. (b) Evolution of T over time during Step F3. (c) Evolution of the mass change in CH_4, H_2O and MH phase during Step F3.

The P- and T- distributions over time in Fig. 21a and 21b, respectively, follow the now-familiar patterns: P is practically time-invariant and uniform within the reactor, and the T-anomaly caused by the warm water injection is attenuated, with T decreasing and becoming more uniform as time advances under the influence of the cooling system. The distributions of S_H and S_A appear practically unchanged in terms of pattern and magnitude during the first 36.0 h covered by Fig. 21c and 21d, respectively, with only a tiny (but still discernible) change of S_H formation and corresponding S_A reduction at the top of the reactor. The pattern of the $S_G$distribution in Fig. 21e appears invariant over time, but with a significant reduction in magnitude as some additional (although small) amount of additional hydrate is formed and some are dissolved into the H_2O. This is evidenced by the changes in the mass of CH_4 and hydrate phase in Fig. 20c. Interestingly, we identified that there is an initial increase of the mass of aqueous phase during Step F3 followed by a decrease after $t = 25.0$ h, which can be attributed to the initial dissolution of CH_4 into the aqueous phase during the continuous cooling process (which increases the mass of aqueous phase) dominating over the slow process of CH_4-hydrate formation reaction (which decreases the mass of aqueous phase) in Step F3. Fig. 21e also reveals that the CH_4 displaced during the water injection in Step I3 does not migrate upward during the much longer Step F3 (as there is no pressure differential and possible dissolution in H_2O) but remains in place and is depleted by forming some additional hydrate. Note that changes in S_A, S_G and S_H continue after the first 36 h depicted in Fig. 21because the hydrate reaction continues (and will continue until $CH_4$is completely exhausted), but the rate is very slow and decelerating, as equilibrium is approached, thus resulting in no discernible visual changes in the saturation distributions for $t > 36.0$ h.

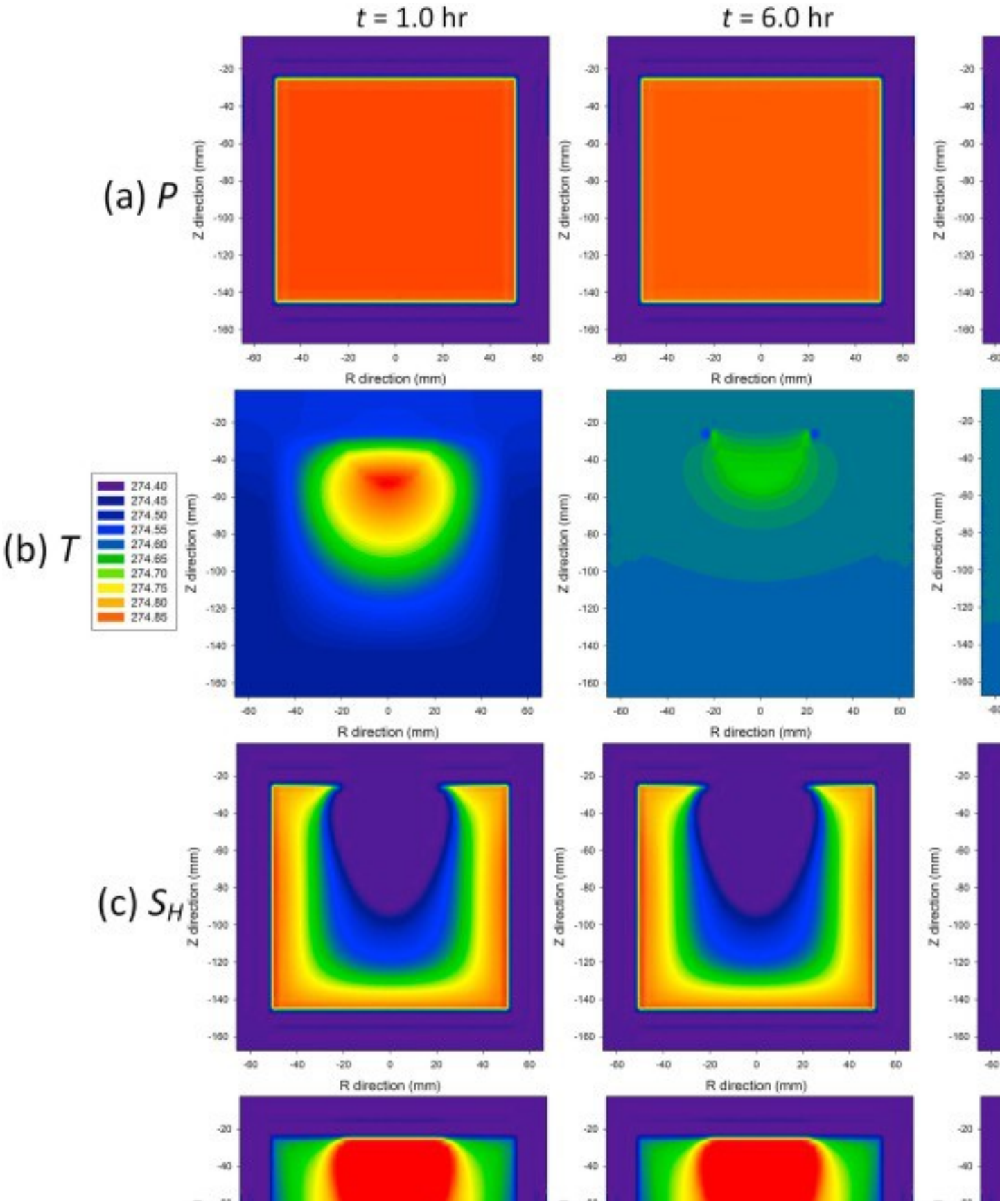
t = 1.0 hr
t = 6.0 hr
(a) P
(b) T
(c) S_H
274.40
274.45
274.50
274.55
274.60
274.65
274.70
274.75
274.80
274.85
Z direction (mm)
R direction (mm)

1. Download high-res image (991KB)
2. Download full-size image

Fig. 21. Evolution of spatial distribution of P, T, S_H, S_A, S_G over time during Step F3. (left T scale for $t = 1.0$ h; right T scale for $t = 6.0$ h and 36.0 h)

5. Summary and conclusions

This study replicates numerically the first part – that of methane hydrate formation – of an earlier experimental study involving hydrate formation and dissociation in a reactor under controlled conditions. Additionally, it is the natural continuation of a subsequent investigation that sought to analyse the experimental results of dissociation by means of numerical simulation based on the initial assumptions of a uniform phase saturation in the rector and an equilibrium reaction of hydrate dissociation [91].

For this study, we used a fine (mm-scale) spatial discretization to describe accurately the geometry of the reactor assembly. Using the TOUGH+HYDRATE v1.5 code [93], the experiment in [63] was simulated by carefully describing the three stages (periods) of the hydrate formation process. The deviations between the experimental data (obtained from the continuous monitoring of $P$and T) and the numerical predictions were minimized through an optimization (history-matching) process that resulted in an excellent agreement between the two data sets, yielded key parameter values and allowed the determination of the model of the hydrate reaction.

The results of this study lead to the following conclusions:

1. Sensitivity analysis and comparison of

   (a) the values of thermal properties obtained from the history-matching process to the known range of such values for a wide variety of geological materials, as well as

   (b) the evolution of the experimental pressures and of the corresponding numerical estimates based on values beyond the upper limits of the thermal property values,

prove conclusively that hydrate formation is a kinetic process, excluding unequivocally the possibility of an equilibrium reaction.

2.

The optimization (history-matching) process of minimization of the deviations between the experimental observations and the numerical predictions indicated conclusively that

(a)

flow properties (more specifically, ϕ and S_{irA}) are only significant during the first water injection (Step I1),

(b)

that the system was insensitive to the intrinsic permeability k of the sand during all steps of the study, and that

(c)

the dominant processes in all subsequent steps (6 in total) in the low-volume reactor are thermal, controlling the hydrate formation that was induced by cooling in Steps F1, F2 and F3, and the temporary and localized dissociation during the injection of warm water in Steps I2 and I3.

3.

The values of the thermal parameters (specific heat and thermal conductivity of the sand) determined from the history-matching process after Step I1 showed that the system behaviour was practically insensitive to the wettability properties of the sand, i.e., the relative permeability, and the capillary pressure due to high absolute permeability, the consequent absence of any wettability-related flow retardation (because of low capillary pressure and high relative permeability), and the limited dimensions/volume of the reactor, which combined to result in very fast initial flows and practically no flow differentials that could lead to slower later flows.

4.

Our simulation studies demonstrate clearly very heterogeneous spatial distributions of the various phases (aqueous, gas and hydrate) at any step of the hydrate-forming process. Actually, uniformity of the initial phase saturation distributions appears to be nearly impossible (especially in multi-stage hydrate formation), as it is precluded by various factors: injector location, gravity/drainage effects, capillary-driven redistribution of phases, the geometry of the reactor, and the non-uniformity of the cooling process. Thus, the frequent assumption of uniform initial phase saturations is not valid for both single- and multi-stage

hydrate formation processes. The assumption of initial phase uniformity in the analysis of laboratory experiments of hydrate dissociation are likely to lead to erroneous results.

5.

The surface area adjustment factor F_A determined from parameter optimization (a key parameter of the kinetic equation of hydration) may not remain constant during the hydrate formation or dissociation reaction and can be function of time. F_A was initially proposed [93] to quantify the area A over which the hydrate reaction occurs. However, it actually acts as an adjustment to the combined product of A(expected to change) and the kinetic reaction constant K_0, which was kept constant in this study at the level specified by Clarke and Bishnoi [110], but is also possible to change over time during the hydration reaction. It is also possible that the time-variable F_A reflects imperfections in the hydrate reaction model, and may also act as a collective curve-fitting factor that masks additional processes not considered in the development of Eq. (2), given that the model of Kim et al. [50] was developed in a stirred tank reactor, that are very different of reality in sandy porous media. Additional experimental work to elucidate this issue is thus needed.

6.

In the absence of experimental equipment capable of providing visual description of the spatial distributions of the various phases in the hydrate-forming reactor (e.g., X-ray CT scanners, MRI and ERT equipment), numerical simulation appears to be a useful and necessary tool for the task. This is necessitated by the numerical simulation studies in this paper, which indicate that the spatial distributions of the various phases are very heterogeneous at any step of the hydrate-forming process by the excess water method.

Acknowledgement

The financial support from the National University of Singapore (R-261-508-001-646 and R-261-508-001-733) is greatly appreciated. Dr. George Moridis, the holder of the ExxonMobil Visiting Chair in the Department of Chemical and Biomolecular Engineering at NUS, extends his thanks to ExxonMobil and NUS for their support. Zhenyuan Yin would like to thank the EDB and LR for the industrial postgraduate programme (IPP) scholarship.

Appendix A. Supplementary material

Download Word document (543KB)Help with docx files

Supplementary data 1.

References

[1]

K.A. Udachin, C.I. Ratcliffe, J.A. Ripmeester**Single Crystal diffraction studies of structure I, II and H hydrates: structure, cage occupancy and composition**

J Supramol Chem, 2 (2002), pp. 405-408

ArticleDownload PDF

[2]

Y.F. Makogon**Hydrates of hydrocarbon**

PennWell Publishing Company, USA (1997)

[3]

E.D. Sloan**Fundamental principles and applications of natural gas hydrates**

Nature, 426 (2003), pp. 353-363

View Record in Scopus

[4]

E.D. Sloan**Gas hydrates: review of physical/chemical properties**

Energy Fuels, 12 (1998), pp. 191-196

CrossRefView Record in Scopus

[5]

A. Gupta, J. Lachance, E.D. Sloan, C.A. Koh**Measurements of methane hydrate heat of dissociation using high pressure differential scanning calorimetry**

Chem Eng Sci, 63 (2008), pp. 5848-5853

ArticleDownload PDFView Record in Scopus

[6]

Moridis GJ. User's manual of the TOUGH+ core code v1. 5: a general-purpose simulator of non-isothermal flow and transport through porous and fractured media. LBNL 6871E. Berkeley (California, USA): Lawrence Berkeley National Laboratory; 2014.

[7]

E.D. Sloan Jr., C.A. Koh**Clathrate hydrates of the natural gases**

(3rd ed.), CRC Press, Boca Raton (FL) (2008)

[8]

G.J. Moridis, T.S. Collett, R. Boswell, M. Kurihara, M.T. Reagan, C. Koh, *et al.***Toward production from gas hydrates: current status, assessment of resources, and simulation-based evaluation of technology and potential**

SPE Reservoir Eval Eng, 12 (2009), pp. 745-771

CrossRefView Record in Scopus

[9]

Trofimuk AA, Cherskiy NV, Tsarev VP. Accumulation of natural gases in zones of hydrate formation in the hydrosphere. Doklady Akademii Nauk SSSR. 1973:931–4.

[10]

K.A. Kvenvolden**Gas hydrates—geological perspective and global change**

Rev Geophys, 31 (1993), pp. 173-187

CrossRefView Record in Scopus

[11]

Y. Makogon**Perspectives of development of gas hydrate accumulations**

Gasovaya Promyshlennost, 3 (1981), pp. 16-18

View Record in Scopus

[12]

K.A. Kvenvolden**Methane hydrate—a major reservoir of carbon in the shallow geosphere?**

Chem Geol, 71 (1988), pp. 41-51

ArticleDownload PDFView Record in Scopus

[13]

G.J. MacDonald**The future of methane as an energy resource**

Annu Rev Energy, 15 (1990), pp. 53-83

CrossRefView Record in Scopus

[14]

K. Kvenvolden**A primer on the geological occurrence of gas hydrate**

Geol Soc, Lond, Special Publ, 137 (1998), pp. 9-30

CrossRefView Record in Scopus

[15]

J.B. Klauda, S.I. Sandler**Global distribution of methane hydrate in ocean sediment**

Energy Fuels, 19 (2005), pp. 459-470

CrossRefView Record in Scopus

[16]

A.V. Milkov**Global estimates of hydrate-bound gas in marine sediments: how much is really out there?**

Earth Sci Rev, 66 (2004), pp. 183-197

ArticleDownload PDFView Record in Scopus

[17]

D. Archer, B. Buffett, V. Brovkin**Ocean methane hydrates as a slow tipping point in the global carbon cycle**

Proc Natl Acad Sci, 106 (2009), pp. 20596-20601
CrossRefView Record in Scopus

[18]

BP. BP statistical review of world energy. Natural gas; 2017. p. 26.

[19]

G.J. Moridis, T.S. Collett, M. Pooladi-Darvish, S.H. Hancock, J.C.Santamarina, R. Boswell, *et al.***Challenges, uncertainties, and issues facing gas production from gas-hydrate deposits**
SPE Reservoir Eval Eng, 14 (2011), pp. 76-112
CrossRefView Record in Scopus

[20]

Z.R. Chong, S.H.B. Yang, P. Babu, P. Linga, X.-S. Li**Review of natural gas hydrates as an energy resource: prospects and challenges**
Appl Energy, 162 (2016), pp. 1633-1652
ArticleDownload PDFView Record in Scopus

[21]

Y.F. Makogon, R.Y. Omelchenko**Commercial gas production from Messoyakha deposit in hydrate conditions**
J Nat Gas Sci Eng, 11 (2013), pp. 1-6
ArticleDownload PDFView Record in Scopus

[22]

Trehu AM, Torres ME, Bohrmann G, Colwell F. Leg 204 synthesis: gas hydrate distribution and dynamics in the central Cascadia accretionary complex; 2006.

[23]

Riedel M, Willoughby E, Chen M, He T, Novosel I, Schwalenberg K, et al. Gas hydrate on the northern Cascadia margin: regional geophysics and structural framework. In: Proceedings of the integrated ocean drilling program; 2006.

[24]

Paull CK. Drilling for gas hydrates: ocean drilling program leg 164. In: Proceedings of the offshore technology conference. Houston (TX): OTC; 1997. p. 1–8.

[25]

Jones E, Latham T, McConnell DR, Frye M, Hunt J, Shedd W, et al. Scientific objectives of the Gulf of Mexico gas hydrate JIP Leg II drilling. Offshore technology conference; 2008.

[26]

Yang S, Zhang H, Wu N, Su X, Schultheiss P, Holland M, et al. High concentration hydrate in disseminated forms obtained in Shenhu area, north slope of South China Sea. In: Proceedings of the 6th international conference on gas hydrates, Vancouver, British Columbia, Canada; 2008.

[27]

Collett TS, Riedel M, Cochran JR, Boswell R, Kumar P, Sathe A. Indian continental margin gas hydrate prospects: results of the Indian National Gas Hydrate Program (NGHP) expedition 01. In: Proceedings of the 6th international conference on gas hydrates, Vancouver, B.C., Canada; 2008.

[28]

Lee SR, Kim DS, Ryu BJ, Bahk JJ, Yoo DG, Kim GY, et al. Recent developments of gas hydrate program in Korea: Ulleung basin gas hydrate drilling expedition 2. In: Proceedings of the 7th international conference on gas hydrates, Edinburgh, Scotland, United Kingdom; 2011.

[29]

Y. Tsuji, H. Ishida, M. Nakamizu, R. Matsumoto, S. Shimizu**Overview of the MITI Nankai trough wells: a milestone in the evaluation of methane hydrate resources**

Resour Geol, 54 (2004), pp. 3-10

CrossRefView Record in Scopus

[30]

T. Collett, J.-J. Bahk, M. Frye, D. Goldberg, J. Husebo, C. Koh, *et al.***Historical methane hydrate project review**

Consortium for Ocean Leadership, Washington D.C. (2013)

[31]

Takahashi H, Yonezawa T, Fercho E. Operation overview of the 2002 Mallik gas hydrate production research well program at the Mackenzie delta in the Canadian Arctic. In: Offshore technology conference, Houston, Texas, USA; 2003.

[32]

Kurihara M, Sato A, Funatsu K, Ouchi H, Yamamoto K, Numasawa M, et al. Analysis of production data for 2007/2008 Mallik gas hydrate production tests in Canada. In: International oil and gas conference and exhibition in China, Society of Petroleum Engineers; 2010. p. 2908–31.

[33]

R.B. Hunter, T.S. Collett, R. Boswell, B.J. Anderson, S.A. Digert, G.Pospisil, *et al.***Mount Elbert gas hydrate stratigraphic test well, Alaska north slope: overview of scientific and technical program**

Mar Pet Geol, 28 (2011), pp. 295-310

ArticleDownload PDFView Record in Scopus

[34]

Schoderbek D, Farrell H, Hester K, Howard J, Raterman K, Silpngarmlert S, et al. ConocoPhillips gas hydrate production test final technical report. United States Department of Energy; 2013.

[35]

Yamamoto K, Terao Y, Fujii T, Ikawa T, Seki M, Matsuzawa M, et al. Operational overview of the first offshore production test of methane hydrates in the Eastern Nankai Trough. In: Proceedings of 2014 offshore technology conference, Houston, Texas, USA; 2014.

[36]

J. Sun, F. Ning, S. Li, K. Zhang, T. Liu, L. Zhang, *et al.***Numerical simulation of gas production from hydrate-bearing sediments in the Shenhu area by depressurising: the effect of burden permeability**
J Unconvent Oil Gas Resour, 12 (2015), pp. 23-33
ArticleDownload PDFView Record in Scopus

[37]

G. Li, X.-S. Li, K. Zhang, B. Li, Y. Zhang**Effects of impermeable boundaries on gas production from hydrate accumulations in the Shenhu Area of the South China Sea**
Energies, 6 (2013), p. 4078
CrossRefView Record in Scopus

[38]

T.S. Collett, A. Johnson, C.C. Knapp, R. Boswell**Natural gas hydrates: a review**
American Association of Petroleum Geologists (2009), pp. 146-219
View Record in Scopus

[39]

Holland M, Schultheiss P, Roberts J, Druce M. Observed gas hydrate morphologies in marine sediments. In: 6th international conference on gas hydrates, Vancouver, B.C., Canada; 2008.

[40]

Dai S, Santamarina JC, Waite WF, Kneafsey TJ. Hydrate morphology: Physical properties of sands with patchy hydrate saturation. J Geophys Res: Solid Earth 2012;117.

[41]

T.J. Kneafsey, H. Lu, W. Winters, R. Boswell, R. Hunter, T.S. Collett**Examination of core samples from the mount Elbert gas hydrate stratigraphic test well, Alaska north slope: effects of retrieval and preservation**
Mar Pet Geol, 28 (2011), pp. 381-393
ArticleDownload PDFView Record in Scopus

[42]

D. Davidson, S. Garg, S. Gough, Y. Handa, C. Ratcliffe, J. Ripmeester, *et al.***Laboratory analysis of a naturally occurring gas hydrate from sediment of the Gulf of Mexico**
Geochimica et Cosmochimica Acta, 50 (1986), pp. 619-623
ArticleDownload PDFView Record in Scopus

[43]

T.J. Kneafsey, G.J. Moridis**X-Ray computed tomography examination and comparison of gas hydrate dissociation in NGHP-01 expedition (India) and Mount Elbert (Alaska) sediment cores: experimental observations and numerical modeling**
Mar Pet Geol, 58 (2014), pp. 526-539
ArticleDownload PDFView Record in Scopus

[44]

Y. Song, F. Yu, Y. Li, W. Liu, J. Zhao**Mechanical property of artificial methane hydrate under triaxial compression**
J Nat Gas Chem, 19 (2010), pp. 246-250
ArticleDownload PDFView Record in Scopus

[45]

W.F. Waite, M.B. Helgerud, A. Nur, J.C. Pinkston, L.A. Stern, S.H. Kirby, *et al.***Laboratory measurements of compressional and shear wave speeds through methane hydrate**
Ann N Y Acad Sci, 912 (2000), pp. 1003-1010
View Record in Scopus

[46]

P. Linga, C. Haligva, S.C. Nam, J.A. Ripmeester, P. Englezos**Recovery of methane from hydrate formed in a variable volume bed of silica sand particles**
Energy Fuels, 23 (2009), pp. 5508-5516
CrossRefView Record in Scopus

[47]

G. Li, B. Li, X.-S. Li, Y. Zhang, Y. Wang**Experimental and numerical studies on gas production from methane hydrate in porous media by depressurization in pilot-scale hydrate simulator**
Energy Fuels, 26 (2012), pp. 6300-6310
CrossRefView Record in Scopus

[48]

M. Yousif, H. Abass, M. Selim, E. Sloan**Experimental and theoretical investigation of methane-gas-hydrate dissociation in porous media**
SPE Reserv Eng, 6 (1991), pp. 69-76
CrossRefView Record in Scopus

[49]

X. Sun, K.K. Mohanty**Kinetic Simulation of methane hydrate formation and dissociation in porous MSedia**
Chem Eng Sci, 61 (2006), pp. 3476-3495
ArticleDownload PDFView Record in Scopus

[50]

H.C. Kim, P.R. Bishnoi, R.A. Heidemann, S.S.H. Rizvi**Kinetics of methane hydrate decomposition**
Chem Eng Sci, 42 (1987), pp. 1645-1653
ArticleDownload PDFView Record in Scopus

[51]

P. Englezos, N. Kalogerakis, P.D. Dholabhai, P.R. Bishnoi**Kinetics of gas hydrate formation from mixtures of methane and ethane**
Chem Eng Sci, 42 (1987), pp. 2659-2666

ArticleDownload PDFView Record in Scopus

[52]

Z. Yin, M. Khurana, H.K. Tan, P. Linga**A review of gas hydrate growth kinetic models**
Chem Eng J, 342 (2018), pp. 9-29
ArticleDownload PDFView Record in Scopus

[53]

M. Khurana, Z. Yin, P. Linga**A review of clathrate hydrate nucleation**
ACS Sustain Chem Eng, 5 (2017), pp. 11176-11203
CrossRefView Record in Scopus

[54]

Z. Yin, Z.R. Chong, H.K. Tan, P. Linga**Review of gas hydrate dissociation kinetic models for energy recovery**
J Nat Gas Sci Eng, 35 (2016), pp. 1362-1387
ArticleDownload PDFView Record in Scopus

[55]

L.A. Stern, D.L. Hogenboom, W.B. Durham, S.H. Kirby, I.-M. Chou**Optical-cell evidence for superheated ice under gas-hydrate-forming conditions**
J Phys Chem B, 102 (1998), pp. 2627-2632
CrossRefView Record in Scopus

[56]

L.A. Stern, S.H. Kirby, W.B. Durham**Peculiarities of methane clathrate hydrate formation and solid-state deformation, including possible superheating of water ice**
Science, 273 (1996), p. 1843
CrossRefView Record in Scopus

[57]

L.A. Stern, S.H. Kirby, W.B. Durham**Polycrystalline methane hydrate: synthesis from superheated ice, and low-temperature mechanical properties**
Energy Fuels, 12 (1998), pp. 201-211
CrossRefView Record in Scopus

[58]

Stern LA, Kirby SH, Durham WB, Circone S, Waite WF. Laboratory synthesis of pure methane hydrate suitable for measurement of physical properties and decomposition behavior. Natural Gas Hydrate Ocean Permafrost Environ 2000:323–48.

[59]

Y.P. Handa, D.Y. Stupin**Thermodynamic properties and dissociation characteristics of methane and propane hydrates in 70-. ANG.-radius silica gel pores**
J Phys Chem, 96 (1992), pp. 8599-8603
CrossRefView Record in Scopus

[60]

R. Anderson, M. Llamedo, B. Tohidi, R.W. Burgass**Experimental Measurement of Methane and Carbon Dioxide Clathrate Hydrate Equilibria in Mesoporous Silica**
J Phys Chem B, 107 (2003), pp. 3507-3514
CrossRefView Record in Scopus

[61]

P. Linga, C. Haligva, S.C. Nam, J.A. Ripmeester, P. Englezos**Gas hydrate formation in a variable volume bed of silica sand particles**
Energy Fuels, 23 (2009), pp. 5496-5507
CrossRefView Record in Scopus

[62]

Priest JA, Rees EV, Clayton CR. Influence of gas hydrate morphology on the seismic velocities of sands. J Geophys Res: Solid Earth 2009;114.

[63]

Z.R. Chong, G.A. Pujar, M. Yang, P. Linga**Methane hydrate formation in excess water simulating marine locations and the impact of thermal stimulation on energy recovery**
Appl Energy, 177 (2016), pp. 409-421
ArticleDownload PDFView Record in Scopus

[64]

Z.R. Chong, Z. Yin, J.H.C. Tan, P. Linga**Experimental investigations on energy recovery from water-saturated hydrate bearing sediments via depressurization approach**
Appl Energy, 204 (2017), pp. 1513-1525
ArticleDownload PDFView Record in Scopus

[65]

S. Falser, S. Uchida, A.C. Palmer, K. Soga, T.S. Tan**Increased gas production from hydrates by combining depressurization with heating of the wellbore**
Energy Fuels, 26 (2012), pp. 6259-6267
CrossRefView Record in Scopus

[66]

B.A. Buffett, O.Y. Zatsepina**Formation of gas hydrate from dissolved gas in natural porous media**
Mar Geol, 164 (2000), pp. 69-77
ArticleDownload PDFView Record in Scopus

[67]

E. Spangenberg, J. Kulenkampff, R. Naumann, J. Erzinger**Pore space hydrate formation in a glass bead sample from methane dissolved in water**
Geophys Res Lett, 32 (2005)

[68]

M. Priegnitz, J. Thaler, E. Spangenberg, C. Rücker, J.M. Schicks**A cylindrical electrical resistivity tomography array for three-dimensional monitoring of hydrate formation and dissociation**
Rev Sci Instrum, 84 (2013), p. 104502
CrossRef

[69]

W.F. Waite, W.J. Winters, D. Mason**Methane hydrate formation in partially water-saturated Ottawa sand**
Am Mineral, 89 (2004), pp. 1202-1207
CrossRefView Record in Scopus

[70]

H.O. Kono, S. Narasimhan, F. Song, D.H. Smith**Synthesis of methane gas hydrate in porous sediments and its dissociation by depressurizing**
Powder Technol, 122 (2002), pp. 239-246
ArticleDownload PDFView Record in Scopus

[71]

S.A. Bagherzadeh, I.L. Moudrakovski, J.A. Ripmeester, P. Englezos**Magnetic resonance imaging of gas hydrate formation in a bed of silica sand particles**
Energy Fuels, 25 (2011), pp. 3083-3092
CrossRefView Record in Scopus

[72]

A. Kumar, T. Sakpal, S. Roy, R. Kumar**Methane hydrate formation in a test sediment of sand and clay at various levels of water saturation**
Can J Chem, 93 (2015), pp. 874-881
CrossRefView Record in Scopus

[73]

Z.R. Chong, A.H.M. Chan, P. Babu, M. Yang, P. Linga**Effect of NaCl on methane hydrate formation and dissociation in porous media**
J Nat Gas Sci Eng, 27 (2015), pp. 178-189
ArticleDownload PDFView Record in Scopus

[74]

P. Linga, N. Daraboina, J.A. Ripmeester, P. Englezos**Enhanced rate of gas hydrate formation in a fixed bed column filled with sand compared to a stirred vessel**
Chem Eng Sci, 68 (2012), pp. 617-623
ArticleDownload PDFView Record in Scopus

[75]

C. Haligva, P. Linga, J.A. Ripmeester, P. Englezos**Recovery of methane from a variable-volume bed of silica sand/hydrate by depressurization**
Energy Fuels, 24 (2010), pp. 2947-2955

CrossRefView Record in Scopus

[76]

T.J. Kneafsey, L. Tomutsa, G.J. Moridis, Y. Seol, B.M. Freifeld, C.E. Taylor,*et al.***Methane hydrate formation and dissociation in a partially saturated core-scale sand sample**

J Petrol Sci Eng, 56 (2007), pp. 108-126

ArticleDownload PDFView Record in Scopus

[77]

W.F. Waite, E. Spangenberg**Gas hydrate formation rates from dissolved-phase methane in porous laboratory specimens**

Geophys Res Lett, 40 (2013), pp. 4310-4315

CrossRefView Record in Scopus

[78]

M. Priegnitz, J. Thaler, E. Spangenberg, J.M. Schicks, J. Schrötter, S.Abendroth**Characterizing electrical properties and permeability changes of hydrate bearing sediments using ERT data**

Geophys J Int, 202 (2015), pp. 1599-1612

CrossRefView Record in Scopus

[79]

Kneafsey TJ, Rees EVL, Nakagawa S, Kwon T-H. Examination of hydrate formation methods: trying to create representative samples. LBNL-4845E. Berkeley (California, USA): Lawrence Berkeley National Laboratory; 2011.

[80]

M. Yang, Z. Fu, L. Jiang, Y. Song**Gas recovery from depressurized methane hydrate deposits with different water saturations**

Appl Energy, 187 (2017), pp. 180-188

ArticleDownload PDFView Record in Scopus

[81]

M. Yang, Z. Fu, Y. Zhao, L. Jiang, J. Zhao, Y. Song**Effect of depressurization pressure on methane recovery from hydrate–gas–water bearing sediments**

Fuel, 166 (2016), pp. 419-426

ArticleDownload PDFView Record in Scopus

[82]

M. Yang, Y. Song, L. Jiang, N. Zhu, Y. Liu, Y. Zhao, *et al.***CO_2 hydrate formation and dissociation in cooled porous media: a potential technology for CO_2 capture and storage**

Environ Sci Technol, 47 (2013), pp. 9739-9746

CrossRefView Record in Scopus

[83]

T.J. Kneafsey, Y. Seol, A. Gupta, L. Tomutsa**Permeability of laboratory-formed methane-hydrate-bearing sand: measurements and observations using X-ray computed tomography**
Spe J, 16 (2011), pp. 78-94
CrossRefView Record in Scopus

[84]
Y. Seol, T.J. Kneafsey**X-ray computed-tomography observations of water flow through anisotropic methane hydrate-bearing sand**
J Petrol Sci Eng, 66 (2009), pp. 121-132
ArticleDownload PDFView Record in Scopus

[85]
J. Stevens, B. Baldwin, A. Graue, G. Ersland, J. Husebo, J. Howard**Measurements of hydrate formation in sandstone**
Petrophysics, 49 (2008), p. 67
View Record in Scopus

[86]
B.A. Baldwin, A. Moradi-Araghi, J.C. Stevens**Monitoring hydrate formation and dissociation in sandstone and bulk with magnetic resonance imaging**
Magn Reson Imaging, 21 (2003), pp. 1061-1069
ArticleDownload PDFView Record in Scopus

[87]
K. Nazridoust, G. Ahmadi**Computational modeling of methane hydrate dissociation in a sandstone core**
Chem Eng Sci, 62 (2007), pp. 6155-6177
ArticleDownload PDFView Record in Scopus

[88]
H. Hong, M. Pooladi-Darvish**Simulation of depressurization for gas production from gas hydrate reservoirs**
J Can Pet Technol, 44 (2005)

[89]
H. Liang, Y. Song, Y. Chen**Numerical simulation for laboratory-scale methane hydrate dissociation by depressurization**
Energy Convers Manage, 51 (2010), pp. 1883-1890
ArticleDownload PDFView Record in Scopus

[90]
X. Ruan, Y. Song, J. Zhao, H. Liang, M. Yang, Y. Li**Numerical simulation of methane production from hydrates induced by different depressurizing approaches**
Energies, 5 (2012), pp. 438-458
CrossRefView Record in Scopus

[91]

Z. Yin, G. Moridis, Z.R. Chong, H.K. Tan, P. Linga**Numerical analysis of experiments on thermally induced dissociation of methane hydrates in porous media**

Ind Eng Chem Res (2017)

[92]

L.K. Thomas, L. Hellums, G. Reheis**A nonlinear automatic history matching technique for reservoir simulation models**

Soc Petrol Eng J, 12 (1972), pp. 508-514

CrossRefView Record in Scopus

[93]

Moridis GJ. User's manual for the hydrate v1. 5 option of TOUGH+ v1. 5: a code for the simulation of system behavior in hydrate-bearing geologic media. LBNL-6869E. Berkeley (California, USA): Lawrence Berkeley National Laboratory; 2014.

[94]

M.B. Kowalsky, G.J. Moridis**Comparison of kinetic and equilibrium reaction models in simulating gas hydrate behavior in porous media**

Energy Convers Manage, 48 (2007), pp. 1850-1863

ArticleDownload PDFView Record in Scopus

[95]

Moridis G. User’s mannual of the MeshMaker v1. 5 code: A mesh generator for domain discretization in simulations of the TOUGH+ and TOUGH2 familes of codes. LBNL 1005134. Berkeley (California, USA): Lawrence Berkeley National Laboratory; 2016.

[96]

G. Moridis**Numerical studies of gas production from methane hydrates**

SPE J, 8 (2003), pp. 359-370

CrossRefView Record in Scopus

[97]

G. Moridis, T. Collett**Gas production from class 1 hydrate accumulations**

J. Kwan (Ed.), Taylor CAdvances in the study of gas hydrates, Springer, US (2004), pp. 83-97

CrossRefView Record in Scopus

[98]

Moridis G, Kowalsky M. Gas production from unconfined class 2 oceanic hydrate accumulations. Economic geology of natural gas hydrate. Netherlands: Springer; 2006. p. 249–66.

[99]

Moridis G, Collett T. Strategies for gas production from hydrate accumulations under various geologic conditions. Report LBNL-52568. Berkeley (California): Lawrence Berkeley National Laboratory; 2003.

[100]

G.J. Moridis, T.S. Collett, S.R. Dallimore, T. Satoh, S. Hancock, B.Weatherill**Numerical studies of gas production from several CH_4 hydrate zones at the Mallik Site, Mackenzie Delta, Canada**
J Petrol Sci Eng, 43 (2004), pp. 219-238
ArticleDownload PDFView Record in Scopus

[101]

G.J. Moridis, J. Kim, M.T. Reagan, S.-J. Kim**Feasibility of gas production from a gas hydrate accumulation at the UBGH2-6 Site of the Ulleung Basin in the Korean East Sea**
J Petrol Sci Eng, 108S (2013), pp. 180-210
ArticleDownload PDFView Record in Scopus

[102]

G.J. Moridis, M.B. Kowalsky, K. Pruess**Depressurization-induced gas production from class-1 hydrate deposits**
SPE Reservoir Eval Eng, 10 (2007), pp. 458-481
CrossRefView Record in Scopus

[103]

Moridis GJ, Reagan MT. Strategies for gas production from oceanic class 3 hydrate accumulations. Offshore technology conference. Houston (Texas): Offshore Technology Conference; 2007.

[104]

H. Stone**Probability model for estimating three-phase relative permeability**
J Petrol Technol, 22 (1970), pp. 214-218
CrossRefView Record in Scopus

[105]

M.T. Van Genuchten**A closed-form equation for predicting the hydraulic conductivity of unsaturated soils**
Soil Sci Soc Am J, 44 (1980), pp. 892-898
CrossRefView Record in Scopus

[106]

B. Ghanbarian-Alavijeh, A. Liaghat, G.-H. Huang, M.T. Van Genuchten**Estimation of the van Genuchten soil water retention properties from soil textural data**
Pedosphere., 20 (2010), pp. 456-465
ArticleDownload PDFView Record in Scopus

[107]

B. Li, X.-S. Li, G. Li**Kinetic studies of methane hydrate formation in porous media based on experiments in a pilot-scale hydrate simulator and a new model**
Chem Eng Sci, 105 (2014), pp. 220-230
ArticleDownload PDFView Record in Scopus

[108]

Y. Liu, I.K. Gamwo**Comparison between equilibrium and kinetic models for methane hydrate dissociation**
Chem Eng Sci, 69 (2012), pp. 193-200
ArticleDownload PDFCrossRefView Record in Scopus

[109]

Moridis GJ, Seol Y, Kneafsey TJ. Studies of reaction kinetics of methane hydrate dissociation in porous media. In: 5th international conference on gas hydrates. Trondheim, Norway; 2005. p. 21–30.

[110]

M. Clarke, P.R. Bishnoi**Determination of the activation energy and intrinsic rate constant of methane gas hydrate decomposition**
Can J Chem Eng, 79 (2001), pp. 143-147
CrossRefView Record in Scopus

[111]

B.S. HnrvrrNcwlv**Quartz: Heat capacities from 340 to 1000 K and revised values for the thermodynamic properties**
Am Mineral, 72 (1987), pp. 273-279

[112]

N. Zhang, X. Yu, A. Pradhan, A.J. Puppala**Thermal conductivity of quartz sands by thermo-time domain reflectometry probe and model prediction**
J Mater Civ Eng, 27 (2015), p. 04015059
CrossRef

[113]

S.X. Chen**Thermal conductivity of sands**
Heat Mass Transf, 44 (2008), p. 1241
CrossRefView Record in Scopus

[114]

M. Clarke, P.R. Bishnoi**Determination of the intrinsic rate of gas hydrate decomposition using particle size analysis**
Ann N Y Acad Sci, 912 (2000), pp. 556-563
View Record in Scopus

[115]

B. Li, Y.-P. Liang, X.-S. Li, L. Zhou**A pilot-scale study of gas production from hydrate deposits with two-spot horizontal well system**

Appl Energy, 176 (2016), pp. 12-21